On the highly swirling flow through a confined bluff-body

Brito Lopes, A. V., Emekwuru, N., Bonello, B. & Abtahizadeh, E.

Original citation & hyperlink:
Brito Lopes, AV, Emekwuru, N, Bonello, B & Abtahizadeh, E 2020, 'On the highly swirling flow through a confined bluff-body', Physics of Fluids, vol. 32, no. 5, 055105. https://dx.doi.org/10.1063/1.5141531

DOI 10.1063/1.5141531
ISSN 1070-6631
ESSN 1089-7666

Publisher: American Institute of Physics

On The Highly Swirling Flow Through A Confined Bluff-Body

A. V. Brito Lopes [1, a)], N. Emekwuru [2,3, b)], B. Bonello [3], E. Abtahizadeh [4]

[1] Centre for Fluid and Complex Systems - Coventry University, Coventry CV1 5FB, UK.
[2] Institute for Future Transport and Cities - Coventry University, Coventry CV1 5FB, UK.
[3] Faculty of Engineering, Environment & Computing - Coventry University, Coventry CV1 5FB, UK.
[4] Department of Mechanical Engineering
Multiphase & Reactive Flows - Eindhoven University of Technology TU/e, Eindhoven 5600 MB, Netherlands
[a)] Correspondence author: britoloa@uni.coventry.ac.uk
[b)] Correspondence author: ab9992@coventry.ac.uk

ABSTRACT

We address highly-swirling, confined-bluff-body-flow evolving through a burner; particularly contributions of the swirling motion to a central-recirculation-zone (CRZ) downstream the injector. Previous studies suggest flame stability reduces in combustors lacking this zone; careful consideration of the CRZ is, thus, desirable. We use Reynolds-Averaged-Navier-Stokes (RANS) and Large-Eddy-Simulation (LES) to simulate the flow; and the influence of the swirl device was included in defining the inflow conditions for LES simulations. We use mean velocity profiles, and turbulence statistics, to test results. There is qualitative agreement between computed and reported experimental data and we document quantitative differences obtained with the RANS models. LES velocity field results are mostly within 3% of the experimental data, better than the latest reported LES data, reinforcing the suitability of our approach. We took advantage of the quality of the LES mesh, which solves 95.6% of the resolved-turbulence-energy, to present the vorticity structures showing the precessing vortex motion on the CRZ boundaries. Anisotropic states of the Reynolds-stress were characterised with the aid of an anisotropy invariant map, a novelty for this type of burner; the turbulence states considerably vary inside the burner, behaving isotropically in the centre of the CRZ whereas axisymmetric turbulence is predominant in the other areas of the CRZ. The results reinforce the importance of applying appropriate turbulence models and inflow conditions for simulations involving confined-bluff-body-flows in order to capture the main flow fields and structures in the CRZ.

I. INTRODUCTION

In the current global scenario of stringent regulations to reduce green-house gas emissions and the dwindling reserves of fossil fuels exacerbated by an increasing consumption of fossil fuel foreseen to rise almost 3 times by 2040, the aviation industry has started to shift towards the use of alternative fuels such as biofuels and blended fossil/biofuels (IATA (2015); ICAO (2017); Bosch et al. (2017)). The complete or partial adoption of alternative fuels will inevitably bring new challenges to the

development of jet engines leading, for instance, to the redesign of the combustion chambers as well as changes to sub-systems such as swirlers, injectors and ignitors (Lefebvre and Ballal (2010)).

The combustion process in aero-gas turbines, more specifically the jet engines, is intrinsically dependent on the high-intensity of the swirling motion inside the combustion chamber. Essentially, it is desirable that, in a jet engine, the combustion is stable, with low pollutant emissions and compact flames which reduce the engine size, hence increasing the aeroplane power-to-weight ratio (Lefebvre (1999)). To achieve such requirements the flow aerodynamics inside the engine have to be precisely designed considering the entire flight envelop in order to guarantee that the flame keeps alight even under adverse conditions that might lead to combustion instabilities such as global or local extinction (Lieuwen (2012), Santhosh and Basu (2016)).

As observed in Figure 1, for a typical large civil aero engine air leaves the diffuser at about 110 m/s before entering the primary zone. Downstream the fuel injector nozzle the incoming swirling air not only generates a recirculation zone that reduces the axial velocity inside the primary zone but also creates an extra component of velocity in the radial direction. Furthermore, in the primary zone under a high level of turbulence intensity, air mixes with the atomised fuel which allows a compact flame to be ignited and become self-sustained. Finally, the hot gases generated in the primary zone are cooled down in the secondary and dilution zones.

Figure 1. Illustration of a modern jet engine combustor showing the swirling flow patterns, where arrows are swirling flow paths.

With regards to the engine combustion processes, the success of any engine design depends on a thorough understanding and analysis of the aerodynamics of the flow, particularly the physics of swirling flow as this plays an important role on the quality of fuel-air mixing and flame instability (Marchione et al. (2009), Mastorakos (2017) and Sánchez et al. (2015)); an ill-design can change the flow inside the combustor, affecting the combustion efficiency, and the heat release (Lefebvre (1999)) and adversely influencing the formation of pollutant emissions such as CO and NO which are sensitive to the intensity of swirl inside the burner (Jalalatian et al. (2019)).

A. Numerical and experimental studies of swirling flows

Due to its relevance in combustion devices, swirling flows either in confined or unconfined burners, have been extensively investigated by computational fluid dynamics (CFD), analytical models and experimental means; indeed, research in this field dates back nearly a century ago (Syred and Beér (1974)). Nonetheless, due to the complex nature of rotating flows, which is further exacerbated in regions of high Reynolds number, the studies of swirling flow are still considered one of the principal challenges in fluid mechanics. The accurate unsteady three-dimensional measurements, modelling of vortex breakdown, acoustic waves and the influence of inlet and geometry conditions remain rather challenging (Xia et al. (1997), Lucca-Negro and Doherty (2001), Lu et al. (2005) and Kevin (2009)).

In a confined burner with highly swirling flow the physics exhibited is quite more complex due to the intricate nature of the vortex breakdown, shear flow, wall boundary layer, corner vortexes as well as flame wall interactions (Gilchrist and Naughton (2003), Greitzer et al. (2007)). There are several types of aerodynamics instabilities that govern a highly swirling flow. For instance, some more common steady and unsteady flow structures are related to axisymmetric and helical disturbances as well as vortex breakdown which are driven by pressure gradients in the radial direction. Such phenomena as reported in (Syred (2006), Billant et al. (1998), Liang and Maxworthy (2005) and Rajamanickam and Basu (2017)) are fundamentally connected to Kelvin-Helmholtz instabilities that appear in the axial and azimuthal shear layers, the Rayleigh instability due to the radial gradient from the azimuthal velocity and finally internal instabilities associated with the Coriolis force.

The design of the burner in terms of confined and unconfined flows is important for the physics of the flow. For instance, Khalil et al. (2016) determined that in confined swirl flows the level of velocity fluctuations inside the burner increases by about 65% compared with the fluctuational velocity field of unconfined flows. Moreover, the turbulent kinetic energy from the confined cases is almost double that of the unconfined case, evidencing the complexities in the turbulence level due to the geometry of the enclosure. They also determined that as a consequence of the confinement, the flow field is shortened in the axial direction and widened in the radial directions. The same trend was observed for the reacting flow measurements by Khalil et al. (2016) hence showing that the aerodynamics effects are extended and accentuated to the burning case.

A summary of previous simulation studies examining swirling flows in confined and unconfined spaces is presented on Table 1.

Table 1. Summary of modelling studies of swirling flows

Study	Details: turbulence models, combustor & flow type	Boundary conditions and Turbulence assessments
(Pierce and Moin 1998)	LES isothermal, low Mach number flow using the Dynamic Sub-grid Scale (SGS) approach of (Moin et al. 1991) in a cylindrical coordinate. A coaxial and confined swirling jet combustor (Sommerfeld et al. 1992; Johnson and Roback 1983).	Inflow conditions are numerically predicted and generated using the body force technique and a uniform radial profile of body force is taken from a priori Poiseuille flow simulation. Turbulence modelling using two different sub-grid models.
(Wang et al. 2004)	LES with a scale-similarity sub-filter (SSM) (Liu et al. 1994). A static swirl generator (with three vane angles 26°, 48° and 66°) is set inside an annular duct.	The inflow conditions for LES followed the same procedures as in (Pierce and Moin 2001; Pierce and Moin 1998). Coherent structures are visualised using 3D vorticity near the vortex breakdown region. Anisotropic turbulence structures are indirectly assessed using the mean velocity profiles, 3D vorticity surfaces and the variance of velocities.
(Freitag and Klein 2005)	Direct Numerical Simulation (DNS). TECFLAM experiments (Schneider et al. 2005). Flow is unconfined.	Mean velocity, constant azimuthal velocity, superimposed pseudo-turbulent fluctuations and pressure are prescribed based on channel flow. Turbulent kinetic energy, power spectrum and pressure iso-surface visualisation of precessing vortex core were investigated.
(Wang et al. 2007)	LES with a compressible Smagorinsky SGS model (Erlebacher et al. 1992). Gas-turbine swirl cup (Cai et al. 2003; Mongia et al. 2001). The flow is confined.	Inflow conditions (mean-flow velocities and temperature) are set using data mapped from previous RANS computations in (Hsiao and Mongia 2003a; Hsiao and Mongia 2003b) while pressure is estimated using one-dimensional calculations. Turbulence assessment is presented in the format of TKE fields and mean velocity profiles. Proper Orthogonal Decomposition (POD) is used for the analysis of the precessing vortex.
(Escue and Cui 2010)	RANS RNG k-ε & RSM models. Pipe-swirling flow (Rocklage-Marliani et al. 2003). Confined flow.	Swirl is generated by imposing the experimental velocity and Reynolds stress profiles at the inlet to the simulation domain. The decay of turbulent kinetic energy as well as plots of Reynolds stresses values are used to assess the model capabilities in resolving the turbulence.
(Benim et al. 2005; 2010)	URANS-RSM and LES using both SGS Smagorinsky (1963) and a low-Reynolds Smagorinsky approach as suggested by Voke (1996). Water test rig equipped with a swirl generator (idealised combustor). Confined flow.	Inflow conditions are generated from steady-state 3D-RANS low-Reynolds number k-ε model simulation which includes a domain decomposition for the inlet section (plenum, slits and swirl generator). The solution is circumferentially-averaged and uniform velocity components are prescribed for the main calculations. Only time-averaged velocity profiles and the rms of the fluctuational velocity are compared using different turbulence models.
(Gui et al. 2010; Xu et al. 2014)	DNS is performed for a confined flow. The theoretical swirl burner is confined.	Inflow conditions are generated using a profile of both the axial and azimuthal velocities at the inlet whereas the azimuthal velocity is changed based on the swirl number. Turbulence data is used to visualise the interaction between twin swirling jets.

As can be deduced from Table 1 a lot of progress has been made with deducing the physics of swirl flows in confined and unconfined spaces using various turbulence models and boundary conditions (interested readers can also see the studies by Abujelala et al. (1984), Wegner et al. (2004), Paik and Sotiropoulos (2010), Talamantes and Maicke (2016), Choi et al. (2018), and Kadu et al. (2019)). However, three issues are observed. Firstly, for most of the numerical studies, the inlet conditions into the combustor are usually set for the conditions downstream after the swirl device; typically, these are inflow conditions prescribing the velocity profiles as obtained from experiments. Another motivation for ignoring the swirl device could be that this reduces the computational costs. However, if experimental inlet data are not available downstream of the swirl device, or, if the inlet conditions are available for only conditions upstream of the swirl device, this option is not possible using CFD. Therefore, the flow through the swirl device has to be considered. Secondly, as the use of LES is now common for strongly swirling flow studies, it is essential that some quality measure of such simulations is presented. This is not trivial as, in theory, the LES is not grid-independent (one of the measures used in assessing RANS simulations); such a case would then be a DNS. Thirdly, the visualisation of the quantitative data from CFD has strongly aided the physical understanding of (for example) the flow structures from the simulations. For strongly swirling flows in confined burners, the visualisation of the turbulence anisotropy has been lacking, mainly because the construction of any visualisation technique can be difficult. The type and quantity of the anisotropy is essential for the development of engineering applications with strongly swirling flows.

This study addresses these three issues hitherto considered in the numerical studies of highly swirling flows in a confined bluff-body burner. The detailed results are presented using Large Eddy Simulation (LES) with the Smagorinsky (1963) Sub-Grid Scale (SGS) model and two distinct steady-state Reynolds-Averaged Navier-Stokes (RANS) turbulence models. Firstly the k-ε (Jones and Launder (1972) and Launder and Spalding (1972)) model using the high-Reynolds number formulation (known as Realizable k-ε) as proposed by Shih et al. (1995), with the viscous-affected layer (including the viscous sub-layer and the buffer layer) modelled using the two-layer approach of Rodi (1991) which is evaluated using the Wolfshtein (1969) variant which is suitable for shear driven flow. Secondly the Reynolds-Stress Modelling (RSM) which is computed using the Linear Pressure-Strain model of Gibson and Launder (1978). The flow before the swirl device is considered in implementing the inlet flow boundary conditions, the quality of the LES is evaluated using the value of the proportion of the resolved motions solved by the mesh and the visual representation of the turbulence anisotropy in the spatial domain has been presented using the Lumley triangle.

The remainder of the paper is structured as follows: section I.B presents a brief review of the reference experimental set-up and flow conditions utilised for the present simulations. Section II presents the mathematical modelling for the RSM, LES and the characterisation of the anisotropy of the Reynolds-stress. Section III presents the numerical approach used, a detailed description of the establishment of inflow boundary conditions for the RANS and LES, and the grid resolution strategies. A brief discussion of the computational issues related to both the classical and Dynamic Smagorinsky models are presented with respect to swirling flows. The results and discussions are presented in section IV, whilst Section V contains the concluding remarks.

B. Reference experimental set-up and flow conditions

Figure 2 shows a representation of the equipment that consists of a lab-scale burner which is one of the benchmark datasets for the International Workshop on Turbulent Combustion of Sprays (TCS) (Giusti (2019), Merci and Gutheil (2014) and Merci et al. (2011)). The burner comprises of a 350 mm annulus channel with 37 mm outer diameter from where air at ambient conditions (1 atm, 288 K) and flow rate of Q_{air} = 500 L/min enters through the swirler device. A bluff-body with a diameter of 19.6 mm is fitted concentrically with the annulus channel. The geometric static swirler device which is located at 41.6 mm upstream of the bluff-body consists of 6 vanes (θ = 60° constant vane angle) with respect to the streamwise flow motion. The air swirl has a clockwise direction when visualised at the nozzle from the combustion region. The blockage rate is 50%. The expanding swirling flow is regarded as a highly confined case (Weber et al. (1990)). For reacting cases, which is not the case investigated herein, there is also a liquid-fuel atomiser centrally located on the top of the bluff-body. The combustion chamber wall is made of quartz which allows for optical access using non-intrusive laser beam; the enclosure has a length of 150 mm ($6D_b$) in the streamwise direction and a square cross-section measuring 95 x 95 mm.

At the annulus channel exit the bluff-body has a wedged top with a diameter D_b = 25 mm which is employed as the reference length. The bulk velocity (U_b= 14.3 m/s) is obtained by the volume flow rate divided by the annular channel passage area, this velocity leads to a high Reynolds number equal to 23,000. This burner was designed to have strong recirculation zones with a geometrical swirl number $S_N = 1.23$ in order to mimic the flow physics commonly encountered in a real gas turbine combustor. When $S_N < 0.6$, the swirl flow can be classified as weak due to the low axial pressure gradient that leads to no formation of internal recirculation zones, whereas $S_N > 0.6$ is classified as strong swirl flow that generates large recirculation zones (Beér and Chigier (1972) and Choi et al. (2018)).

Figure 2. The Cambridge swirl-stabilised lab-scale burner. The cold flow tests were carried out with the burner in the vertical position with the bulk flow moving in the streamwise direction (Y-axis). All dimensions are in mm (Sidey et al. (2017)).

We test the reported simulation techniques against the experimental data reported in Sidey et al. (2017) and Cavaliere (2013a), using the burner in Figure 2, for single-phase non-reacting flow using air only as the working fluid. Radial distributions of mean velocity and rms of the velocity fluctuations (axial, radial and azimuthal) values were measured using 1-D Laser Doppler Anemometry (LDA). Experimental data were generated and presented in terms of the azimuthal, axial and radial (X- Y- Z) coordinates as indicated in the schematic in Figure 2. The origin of the coordinate system is at the centre on the top of the bluff-body and has coordinate values (0, 0, 0) mm. The radial direction (Z-axis) is normalised by the characteristic diameter (D_b). In the streamwise direction (Y-axis) measurements were carried out for a total of 9 different stations. The first and nearest sampling station is at $y = 8$ mm. Further downstream stations are located at $y = 13$, 18, 23, 28, 33, 38, 80 and 117 mm which is close to the outlet of the burner, as can be seen in Figure 2.

A total of 200,000 data samples were recorded from all the measurement locations with a statistical uncertainty of 1-3%. The bulk velocity was measured with an uncertainty of 3%. The uncertainty analysis followed by a detailed description of the LDA system can be found in Sidey et al. (2017) and Cavaliere (2013a, b). The focus of the measurements was the central recirculation zone (CRZ), therefore, measurements inside the annulus channel and the near-wall regions were not carried out. Thus, most of the radial measurements are available only for $-1.8 < Z/D_b < 1.8$ which do not include near walls.

II. MATHEMATICAL MODELLING

A. Reynolds-Stress Modelling (RSM)

The Reynolds-stress transport equation can be represented as:

$$\frac{\partial}{\partial t}(\rho \boldsymbol{R}) + \nabla.(\rho \boldsymbol{R}\overline{\boldsymbol{v}}) = \nabla.\mathbf{D} + \mathbf{P} - \frac{2}{3}\rho \mathbf{I}\Upsilon_M + \varphi + \varepsilon \tag{1}$$

The tensor $\boldsymbol{R}$ is the Reynolds-stress term that appears in the momentum equation as a result of the Reynolds-averaging process, $\overline{\boldsymbol{v}}$ is the mean velocity field and Υ_M is the dilatation dissipation which is modelled according to Sarkar and Lakshmanan (1991). Tensor **D** is the Reynolds-stress diffusion term which is computed from an isotropic form for the turbulent diffusion (Lien and Leschziner (1994)) as in equation (2):

$$\mathbf{D} = \left(\mu + \frac{\mu_t}{\sigma_k}\right)\nabla \mathbf{R} \tag{2}$$

The turbulent viscosity μ_t is computed as in equation (3):

$$\mu_t = \rho C_\mu \frac{k^2}{\varepsilon} \tag{3}$$

The turbulent kinetic energy is computed as in equation (4):

$$k = \frac{1}{2} tr(\boldsymbol{R}) \tag{4}$$

The term **P** in equation (1) is the turbulent production which does not require modelling and it is directly obtained by:

$$\mathbf{P} = -\rho(\boldsymbol{R}.\nabla\overline{\boldsymbol{v}}^{\boldsymbol{T}} + \nabla\overline{\boldsymbol{v}}.\boldsymbol{R}) \tag{5}$$

The isotropic turbulent dissipation rate evolves according to:

$$\frac{\partial}{\partial t}(\rho\varepsilon) + \nabla.(\rho\varepsilon\overline{\boldsymbol{v}}) = \nabla.\left[\left(\mu + \frac{\mu_t}{\sigma_\varepsilon}\right)\nabla\varepsilon\right] + \frac{\varepsilon}{k}\left[C_{\varepsilon 1}\left(\frac{1}{2}tr(\boldsymbol{P}) + \frac{1}{2}C_{\varepsilon 3}tr(\boldsymbol{G})\right) - C_{\varepsilon 2}\rho\varepsilon\right] \quad (6)$$

All the modelling constant coefficients adopted herein are summarized in Table 2. The Linear Pressure-Strain (LPS) model applied in the present simulation is solved as:

$$\varphi = \varphi_s + \varphi_r + \varphi_{1w} + \varphi_{2w} \quad (7)$$

The slow pressure-strain term (φ_s) and the rapid pressure-strain (φ_r) are computed as follows:

$$\varphi_s = -C_1\rho\frac{\varepsilon}{k}\left(\boldsymbol{R} - \frac{2}{3}k\mathbf{I}\right) \quad (8)$$

$$\varphi_r = -C_2\left[\boldsymbol{P} - \frac{1}{3}\mathbf{I}\,\mathrm{tr}(\boldsymbol{P})\right] \quad (9)$$

The slow (φ_{1w}) and rapid (φ_{2w}) wall-reflection terms are modelled following equations (10) and (11) respectively,

$$\varphi_{1w} = \rho C_{1w}\frac{\varepsilon}{k}\left[(\boldsymbol{R}:\boldsymbol{N})\boldsymbol{I} - \frac{3}{2}(\boldsymbol{R}\,.\boldsymbol{N} + \boldsymbol{N}\,.\boldsymbol{R})\right]f_w \quad (10)$$

$$\varphi_{2w} = C_{2w}\left[(\varphi_r:\boldsymbol{N})\boldsymbol{I} - \frac{3}{2}(\varphi_r\,.\boldsymbol{N} + \boldsymbol{N}\,.\varphi_r)\right]f_w \quad (11)$$

wherein the tensor $\boldsymbol{N} = \boldsymbol{n}\otimes\boldsymbol{n}$ where $\boldsymbol{n}$ is the normal unit vector.

The term f_w is a near-wall scalar function applied to account for the transfer of energy from the flow in the streamwise direction to the normal wall direction due to the pressure field, and is computed thus:

$$f_w = min\left(\frac{l}{l_\varepsilon}, f_w^{max}\right) \quad (12)$$

In equation (12), the term $l = k^{3/2}/\varepsilon$ is the characteristic turbulence length scale and $l_\varepsilon = C_l d$ is the near-wall equilibrium length scale (the quantity d is the distance to the wall and C_l is a model coefficient). According to Gibson and Launder (1978) and Shir (1973) f_w^{max} = 1 very close to the wall.

The basis for the determination of the model constants in Table 2 and their implications on the flow field modelling can be found in Gibson and Launder (1978).

Table 2. Turbulence modelling constant coefficients

Linear Pressure-Strain						
C_1	C_2	C_{1w}	C_{2w}	$C_{\varepsilon 3}{}^{*}$	C_l	f_w^{max}
1.8	0.6	0.5	0.3	0.5	2.5	1
k-ε						
σ_k	σ_ε	$C_M{}^{**}$	C_s	$C_{\varepsilon 1}$	$C_{\varepsilon 2}$	C_μ
0.82	1	2	0.2	1.44	1.92	0.09

*Computed according to Henkes et al. (1991) and ** Sarkar and Lakshmanan (1991)

B. LES conservation equations

In contrast to RANS equations, in LES the equations are obtained by a spatial-filtering process instead of an averaging process. Large scales of turbulent motions are directly resolved while the small-scale which are hypothesised to have a universal isotropic behaviour are modelled (Deardorff (1970)). The spatial-filtering process of a solution variable φ is decomposed in a filtered variable $\bar{\varphi}$ and a sub-grid scale term. The formalism for the filtered variable is shown below (Denaro (2011)) :

$$\bar{\varphi}(\boldsymbol{x}, t; \Delta) = \int_{R^3} G(\boldsymbol{x} - \boldsymbol{x}'; \Delta)\varphi(\boldsymbol{x}', t)d\boldsymbol{x}' \equiv G * \varphi \tag{13}$$

(*) represents the convolution product between the kernel filter and the unresolved term applied in the entire computational domain.

The high-frequency scales (smaller eddies) are removed by the implicit spatial-filtering kernel $G(\boldsymbol{x} - \boldsymbol{x}'; \Delta)$ that has a filter width $\Delta = \left(\Delta_x \Delta_y \Delta_z\right)^{1/3}$. Since a spatial filter was imposed and taking into account that the nature of the Navier-Stokes equations makes it possible to associate a characteristic time scale for each length scale of turbulence motion, it means that an implicit time filtering is automatically imposed (Sagaut (2006)).

The Newtonian incompressible conservation equations can be written in vector notation as:

$$\frac{\partial \rho}{\partial t} + \nabla.(\rho\bar{\boldsymbol{v}}) = 0 \tag{14}$$

$$\frac{\partial}{\partial t}(\rho\bar{\boldsymbol{v}}) + \nabla.(\rho\bar{\boldsymbol{v}}\otimes\bar{\boldsymbol{v}}) = -\nabla.\bar{p}\boldsymbol{I} + \nabla.(\mathbf{T} + \boldsymbol{T_{SGS}}) \tag{15}$$

The sub-grid scale (SGS) stresses can be represented as:

$$\boldsymbol{T}_{SGS} = 2\mu_t \boldsymbol{S} - \frac{2}{3}(\mu_t \nabla . \overline{\boldsymbol{v}})\boldsymbol{I} \tag{16}$$

$\boldsymbol{S}$ is the strain rate tensor now computed from the resolved mean velocity field $\overline{\boldsymbol{v}}$. The sub-grid scale turbulent viscosity (μ_t) in equation (16) must be described by a sub-grid scale model. The Smagorinsky (1963) SGS model applied herein provides the mixing-length type formula for the sub-grid scale turbulent viscosity as:

$$\mu_t = (C_s f_v \Delta)^2 \boldsymbol{S} \tag{17}$$

The Smagorinsky coefficient (C_s) in equation (17) is not universal and depends on the local flow conditions. The term $C_s\Delta$ is the Smagorinsky length-scale which is analogous to the mixing length hypothesis. Herein we adopted the value of C_s = 0.1 as suggested by Lilly (1967) and also used by Proch et al. (2015). In the present case our LES analysis is carried out with near-wall modelling (so called LES-NWM) by means of the van Driest damping function (f_v) which is applied for proper results in the wall-bounded flow (Piomelli et al. (1988)), it reads as:

$$f_v(y^+) = 1 - exp[-(y^+/A^+)^3] \tag{18}$$

The model coefficient A^+ is ascribed the value of 25 (Piomelli et al. (1988)) and the non-dimensional wall distance is computed as $y^+ = u^* d/\nu$ where $u^*$is the friction velocity computed from the wall shear stress at the nearest wall face, d is the distance to the wall and ν is the kinematic viscosity.

C. The characterisation of the Reynolds-stress anisotropy

The level of anisotropy of the Reynolds-stresses was assessed by using the Lumley-invariant triangle (Lumley and Newman (1977); Lumley (1979)) and graphically plotted as suggested by Pope (2000). In this diagram all the Reynolds-stresses that can occur in a realisable turbulent flow correspond to a point inside the Lumley triangle representing, therefore, all the states of turbulence which have to be contained within the triangle.

The Reynolds-stresses anisotropy can be characterised in a more convenient manner by its six components b_{ij} of the normalised anisotropy tensor in a dimensionless format following Pope's notation (Pope (2000)):

$$b_{ij} = \frac{\langle u_i u_j \rangle}{\langle u_l u_l \rangle} - \frac{1}{3}\delta_{ij} = \frac{a_{ij}}{2k} \tag{19}$$

In equation (19) repeated indices are summed, the temporal average is represented by $\langle\, . \,\rangle$ and k is the turbulent kinetic energy as in equation (4).

Since the normalised anisotropy tensor (b_{ij}) has zero trace, it has only two invariants, therefore the states of turbulence can be represented using only two variables (Lumley (2007)) denoted here by ξ and η, which allow a convenient graphical representation (Simonsen and Krogstad (2005), Emory and Iaccarino (2014)). The definitions of ξ and η following Pope (2000) are:

$$6\eta^2 = -2II_b = {b_{ii}}^2 = b_{ij}b_{ji} \tag{20}$$

$$6\xi^3 = 3III_b = {b_{ii}}^3 = b_{ij}b_{jl}b_{li} \tag{21}$$

The sum of the eigenvalues (λ_1, λ_2 and λ_3) of b in equations (20) and (21) is zero which means that the principal axis of b_{ij} is:

$$\tilde{b}_{ij} = \begin{bmatrix} \lambda_1 & 0 & 0 \\ 0 & \lambda_2 & 0 \\ 0 & 0 & -\lambda_1 - \lambda_2 \end{bmatrix} \tag{22}$$

Where $\tilde{b}$ is the tensor b in the base of the principal axes. In addition, there is a relation between ξ and η with the eigenvalues of b_{ij} through

$$\xi^3 = -\frac{1}{2}\lambda_1\lambda_2(\lambda_1 + \lambda_2) \tag{23}$$

$$\eta^2 = \frac{1}{3}(\lambda_1^2 + \lambda_1\lambda_2 + \lambda_2^2) \tag{24}$$

The three eigenvalues (λ_1, λ_2 and λ_3) indicate the strength of the fluctuating velocity components for any specific point in the flow field both in space and time. The three invariants of a second rank tensor can be related through the Cayley-Hamilton theorem which states that every second rank tensor has its own characteristic equation (Spencer (1971)). For this work, the special states of the Reynolds-stress have been constructed and presented in Table 3, which is adapted from Pope (2000) and Simonsen and Krogstad (2005). This table leads to the construction of the Lumley-Pope diagram presented and discussed in the results section, section IV-E.

Table 3. States and shape of the Reynolds-stress tensor. The images are reproduced with permission from Simonsen, A. J. and Krogstad, P. 'Turbulent Stress Invariant Analysis: Clarification of Existing Terminology'. Physics of Fluids 17 (8), 088103 (2005), with the permission of AIP Publishing.

State of turbulence	Invariants	Eigenvalues of b	Shape of stress tensor	Illustration of shapes
Isotropic	$\xi = \eta = 0$	$\lambda_1 = \lambda_2 = \lambda_3 = 0$	Sphere (isotropic)	Figure t3d1
Two-component axisymmetric	$\xi = -\frac{1}{6}, \eta = \frac{1}{6}$	$\lambda_1 = \lambda_2 = \frac{1}{6}$	Disk 2 component axi	Figure t3d2
One-component	$\xi = \frac{1}{3}, \eta = \frac{1}{3}$	$\lambda_1 = \frac{2}{3}$, $\lambda_2 = \lambda_3 = -\frac{1}{3}$	Line 1 component	Figure t3d3
Axisymmetric (one large eigenvalue)	$\eta = \xi$	$-\frac{1}{3} \leq \lambda_1 = \lambda_2 \leq 0$	Prolate spheroid axisymmetric, $\xi < 0$	Figure t3d4
Axisymmetric (one small eigenvalue)	$\eta = -\xi$	$0 \leq \lambda_1 = \lambda_2 \leq \frac{1}{6}$	Oblate spheroid axisymmetric, $\xi > 0$	Figure t3d5
Two-component	$\eta = \left(\frac{1}{27} + 2\xi^3\right)^{1/2}$ $F(\xi, \eta) = 0$	$\lambda_1 + \lambda_2 = \frac{1}{3}$	Ellipse 2 component axisymmetric	Figure t3d6

III. MODELLING METHODOLOGY

A. Computational Grids

The application of the inlet boundary conditions by considering the flow before the swirl device requires the simulation of the full geometry which will inevitably lead to the simulation of the flow through-the-vane (TTV). Figure 3 illustrates the full domain used to generate the inlet conditions herein.

Figure 3. Full 3D CAD geometry with the main control volumes (CV) used for meshing. (Bonello (2018)).

Figure 4 illustrates the mesh structure used for the simulation without the swirl device. The inlet starts at y = 34.1 mm upstream of the bluff-body thus avoiding the recirculating flow in the void area formed between the top of the swirl device and the bottom of the hub interface (see Figure 7 - interface recirculating flow) and also allowing enough relaxation distance for the development of the LES inflow synthetic eddies.

Figure 4. A) Full 25 structured blocks and internal blocking splitting. B) Fine hexahedral mesh without swirl device for both RANS and LES studies. C) Zoom-in on the bluff-body exiting area showing the meshing distribution.

B. Solutions Method

The solver StarCCM+ (Siemens (2018)) uses the finite-volume method for the discretisation in time and space of the incompressible Navier-Stokes equations introduced in section III. Momentum and continuity equations are linked using a predictor-corrector approach by means of the SIMPLE pressure-velocity coupling algorithm along with the Rhie-and-Chow dissipation correction term to prevent the pressure-correction equation suffering from unphysical checker boarding of pressure. All the simulations were carried out using the Linux High Performance Computer facility of Coventry University.

C. Numerical Discretisation and Solution Strategy

For RANS the convective flux is approximated using a 2nd order midpoint rule scheme, in other words, the flux integral is evaluated as the product of the scalar property at the cell face centre and the cell face area. In the case of the RSM a reduction in under-relaxation parameters is also applied on the pressure, velocity and the Reynolds-stress equations in order to mitigate convergence issues; however, it comes at a higher computational cost. For LES the convective flux is solved using a 2nd order bounded central-differencing (BDS) that consists of a blend of the unconditionally bounded 1st order upwind differential scheme (FOU), the 2nd order differential upwind scheme (SOU) and a central-differencing scheme (CDS); the BDS scheme applied herein is blended with the FOU/SOU schemes in order to improve its numerical stability. We also tested a 3rd order MUSCL scheme however the computational time became quite costly and no significant accuracy improvement computing the turbulent kinetic energy field was found, thus we kept the 2nd order scheme for all the simulations.

For LES the transient term is discretised using an implicit 2nd order scheme and a constant time step is used. The choice of a proper time step in unsteady simulations involving swirling flows and complex geometry, for which analytical or DNS data is not available, is of fundamental importance. In order to test and define an accurate time step a pragmatic approach using different time steps was tested in the context of the present simulation. The integral time scale for this burner is $T = \frac{D_b}{U_b} = 1.75 \times 10^{-3} s$. We started our tests solving this characteristic time scale from Δt = 0.01T, with ten

steps, ending at Δt = 0.5T. The use of a too large time step O ($10^{-4}s$) although possible (implicit solver used), led to some convergence issues due to a higher CFL number and the rms of the velocity fluctuations did not converge satisfactorily. On the other hand, by using a too small Δt = O ($10^{-6}s$) our computations became computationally prohibitive considering the computational resource available in the framework of this paper. We found that for a Δt = 10^{-5}s and the fine mesh (Figure 6 (b)) a favourable convective CFL number smaller than 1.0 in the combustor area was achieved hence assuring good numerical stability and accuracy. Each time-step was solved considering 20 inner-iterations in order to ensure asymptotical convergence at the end of each time step based on criteria of 3-4 order of reduction in residuals.

The total computational period for each case was 10T, where the first 5T is used for the initial settling and flow development while the remaining 5T is used for time-averaging; the simulation stopped after 10T because the flow did not show any substantial change in structure. Therefore, sampling for longer time, i.e. using between 6-8T did not improve the matching against experimental data, only small changes in symmetry are observed. In highly swirling flows convergence criteria based on the reduction of the residuals solely, may not be seen as guarantee of a fully converged solution. In order to test for statistical convergence a series of probes and monitors containing the co-variance of velocities are strategically placed inside the burner (preferably in the shear layer where the flow is uncertain and fluctuates vigorously), the maximum and minimum oscillations are monitored until a flattened behaviour is achieved, this is checked at the end of each sampling period. In addition to this the swirl number, which contains the ratio of the linear and angular momentum, is also used as a convergence criterion along with a balance of mass between the inlet and outlet. Both parameters are checked along with the residuals of the iterative process. Finally, the data is compared against experiments. The results are presented in section IV.

D. Boundary conditions

The inlet boundary conditions for the RANS models are straightforwardly generated using Dirichlet conditions at the inlet (bulk velocity, pressure, temperature and turbulence intensity are known). In the absence of experimental data at the inlet inflow, special attention has to be given to the initialisation of the ambient inflow primary-variable required for the k-ε two-layer model which herein is computed based on the recommendation from Spalart and Rumsey (2007). Usually an unrealistic choice of this value may lead to significant convergence issues during the initial iterations. The outlet conditions for both RANS and LES are defined as a pressure-outlet type, it means that the pressure computed at the outlet is interpolated from the pressure field inside the domain. Finally, the walls are no-slip and adiabatic.

The simulations involving the full domain also allow for the assessment of the influence of the outlet boundary conditions. It is known that the exit boundary conditions for such flow conditions have a considerable influence on the predicted flow features (Pierce and Moin (1998)) and our initial exploratory simulations also indicated this. It was therefore necessary to extrude the outlet domain by 100 mm ($4D_b$) in the axial length in order to alleviate the backflow effects and ensure overall mass conservation. To reinforce these, two outlet boundaries (non-reflecting and extrapolated pressure from the interior domain) were applied and the good match (Section IV. B) of the RSM and

LES simulations with experimental data for the mean axial velocity profile near the outlet of the burner is evidence of the appropriateness of this approach.

E. LES inflow initialisation

In many numerical studies involving burners, the swirl devices are not usually included in the assessments. This could be because experimental data are usually measured downstream after the swirl device, and the computational costs of including them are prohibitive. However, if the experimental data are only available upstream before the swirler, and DNS data is unavailable, a means of estimating the inlet conditions to the burner chamber has to be ascertained for computational studies.

Typically computational studies (Escue and Cui (2010); Freitag and Klein (2005); Kadu et al. (2019); Paik and Sotiropoulos (2010); Pierce and Moin (1998)) have considered the flow conditions after the swirl device by using constant profiles of the velocity values for inflow initialisation which usually requires a tuning-in process to match numerical and experimental data, consequently the influence of the swirl device on the flow physics history is lost and predictive capability of the turbulence modelling can be undermined. Others, such as Wang et al. (2007) have used published inflow conditions (mean velocity profiles and temperature) from resolved RANS k-ε simulations in order to initialise inflow LES therefore making the issues more tractable and computationally feasible; Benim et al. (2010) also used a simple and inexpensive low-Reynolds RANS k-ε model to generate inlet conditions from a decomposed domain.

However, simulating the full domain, including the swirler, would enable a complete characterisation of the flow features, including all the influences on the flow structure from the various components and structure of the burner, which cannot be derived from the methods employed in previous studies. For the present studies, the generation of turbulence inflow is based on the Synthetic Eddy Method (SEM) of Jarrin et al. (2006). The turbulent flow field is seen as a superposition of coherent structures (spinning eddies) at the inlet. The synthetic eddies generated at the inflow are convected and recycled in the computational domain with the mean inflow velocity. SEM requires that both the mean velocity profile and the turbulence intensity are known a priori, we have obtained these data from a RANS simulation of the full computational domain involving the swirler (section IV. A). Sections III. F, and IV further confirm the robustness of this approach.

The turbulent structures must be allowed to develop naturally as the turbulent eddies are convected downstream the annulus channel. In order to allow the development into physically representative turbulent structures the synthetic eddies require a relaxation distance from the inlet. We have carried out a parametric study in order to check the sensitivity of the turbulent inflow field based on both the inlet distance and the turbulent intensity, and ensure that sufficient distance is given between the inflow boundary and the region of interest for testing it at the first measurement station (y = 8 mm; see Figure 2). Thus, parametric analysis involving varying the level of turbulence intensity (±15 %) is used. Varying the turbulence intensity changes the length-scale of the inflow eddies coming into the domain. The calculated flow field, mean velocities and the rms of the three component of velocity fluctuations, remained insensitive to the variations on the intensity of the incoming turbulence structures, mostly because the effects of the

high anisotropy and turbulent field observed at y = 8 mm is due to the shear layer interactions in the CRZ.

F. The Dynamic-Smagorinsky model test

The use of a more advanced SGS model such as the Dynamic Smagorinsky model (Germano et al. (1991)) is often commented in the literature (Wang et al. (2007)) as a means of improving accuracy, usually on the basis that the original Smagorinsky SGS model has some shortcomings. For some flow types the main drawback lies in the Smagorinsky constant (C_s) which is not universal and is usually obtained from canonical flows while the Dynamic Smagorinsky uses a dynamical variation of C_s based on a test-filtering procedure, usually it comes at a higher computational cost. Direct comparison for these two sub-grid models in highly swirling flow is often not carried out. Herein, we decided to check the accuracy of both SGS models in the case of our highly swirling flow case. Both SGS models were tested using the same mesh, boundary and initial conditions. The results depicted in Figure 5 were obtained at the first measurement station y = 8 mm. Table 3 shows the maximum absolute velocity difference (MAVD) encountered in the domain, the average of the mean velocity difference (AMVD) and how much it compares to the bulk velocity. For brevity, the principal conclusion here is that for this type of flow the Dynamic-Smagorinsky model does not show any significant difference over the original Smagorinsky model. The solutions are generally similar and marginal differences are found in computed time-averaged velocities, with the percentage in the range of 0.98-3.16% of the bulk velocity which is in the experimental error range of 1-3%.
Thus, the use of the original Smagorinsky SGS is justified. The Dynamic Smagorinsky model, which is not a feature of this present study, was therefore not pursued further.

Figure 5. Radial distribution of time-averaged velocity profile at the first measurement station y = 8 mm, predicted using the original Smagorinsky and the Dynamics Smagorinsly models.

Table 4. Differences in mean velocity computations using the Dynamic and original Smagorinsky model. The Smagorinsky constant is $C_s = 0.1$

Mean velocity	MAVD (m/s)	AMVD (m/s)	Percentage of the bulk velocity (%)
V (Axial)	2.5380	0.4533	3.1699 %
U (Swirl)	1.7183	0.1970	1.3778 %
W (Radial)	1.1535	0.1411	0.9867 %

G. Assessment of Mesh Resolution

One of the ways to determine the quality of a chosen mesh for LES is by using the so-called Pope's $M(\boldsymbol{x}, t)$ criterion as suggested by Pope (2004). This measure, as defined by equation (25), is used to compute how much of the resolved motions are being solved

by the mesh and how much are being modelled by the SGS model therefore it can be used as a criterion for solution-adaptive gridding. It requires the computation of both the instantaneous turbulent kinetic energy in time and space as well as the amount of turbulent energy being solved by a particular SGS model, in this case the chosen Smagorinsky SGS model.

$$M(\boldsymbol{x},t) \equiv \frac{k_{SGS}}{(k_{SGS}+k_{res})} \tag{25}$$

$$k_{res} = \frac{1}{2}\langle (u_i - \langle u_i \rangle)(u_i - \langle u_i \rangle) \rangle \tag{26}$$

In equation (25) the sub-grid scale turbulent kinetic energy is modelled as $k_{SGS} = C_t \frac{\mu_t}{\rho} S$ where $C_t = 3.5$ is computed following recommendations in Vreman et al. (1994), the resolved turbulent kinetic energy (k_{res}) is defined by equation (26), where $\langle\,.\,\rangle$ denotes temporal average.

$M(\boldsymbol{x},t)$ is a value that lies between 0 and 1. The best-case scenario, yet the most computationally expensive corresponds to M = 0 which is a DNS, and M = 1 to RANS. The smaller the value of $M(\boldsymbol{x},t)$ the more energy contained in the turbulent motions are solved which can be achieved by applying smaller values of Δ, in other words, refining the mesh. For practical problems involving mixing shear layers a value of $M = 0.2$ which corresponds to 80% of the turbulent kinetic energy being captured by the mesh is usually aimed for and acceptable based on a compromise relation of computational cost and accuracy targets (Matheou et al. (2010; 2014)).

Figure 6 shows the mesh analysis that was carried out considering both an intermediate (1 million) and a fine (7 million elements) mesh. The size of the present fine mesh is comparable to the size of mesh cells generated for this same burner by Tyliszczak et al. (2014), Zhang (2015) and Giusti (2017) that have focused only on the reacting flow situations. Several areas of critical meshing are represented in Figure 6 by: A (bottom and side walls), B (corner recirculation), C (central recirculation zone) and D (expansion and conical shear layer). Both meshes are capable of solving a considerable amount of turbulent kinetic energy but the fine mesh (Figure 6 (b)) is substantially refined close to the top of the bluff-body, combustion chamber corners and in the expansion of the annulus which are zones of intense shear flow as discussed in section IV-B. The fine mesh (Figure 6 (b)) is capable of solving more than 95.6% of the turbulence resolved energy in regions C and D and 90% in region (B) but requiring about 7 times more computational time than the intermediate mesh. The intermediate mesh was not pursued further since the fine mesh was found to be suitable for the mean and rms velocity and TKE resolution; furthermore increasing the mesh refinement was not possible due to the computational resources required; reducing the grid space by half would increase the required memory and CPU time by a factor of 8 and 16 respectively (Pope (2004)).

(a) **(b)**

Figure 6. Combustion chamber symmetric plane coloured by Pope's $M(\boldsymbol{x}, t)$ criterion. (a) intermediate mesh and (b) fine mesh.

The void areas in Figure 6 (a) (represented by A) are clearly under-resolved in the intermediate LES analysis. The zones downstream the top of the bluff-body (encompassed by zone C and D in Figure 6 (a)) in the streamwise direction is better resolved by the fine mesh which is a requirement for prospect combustion simulations. Even though the intermediate mesh in Figure 6 (a) is lacking in resolution for areas A, B, C and D it is still a good starting point for defining the areas for mesh refinement and also for some exploratory studies.

IV. RESULTS AND DISCUSSION

A. Inlet Conditions Computation (Flow Through Vanes)

As discussed previously the inlet boundary conditions used as inflow conditions in the domain without the swirler device are initialised from simulations using the entire combustor domain (through-the-vane approach). The full domain simulations accompanied with grid-independent validation were carried out in Bonello (2018) using the Realizable k-ε model. Since experimental data is not available at the annulus channel, we had to assure that this inflow is reliable. Therefore, we carried out *a posteriori* analysis using LES with the Smagorinsky SGS model in order to check the validity of the inlet inflow conditions generated using the k-ε model. Figure 7 shows the mean swirl and axial velocities contour results from the flow through-the-vanes simulation. It can be seen that the flow moves smoothly from the inlet and is greatly unchanged in the annulus; once it reaches the vanes the flow changes direction generating the azimuthal/swirl velocity component while the axial velocity is deflected in the radial direction towards the outer wall. The highest concentration and gradient of both axial and swirl velocities, considering the entire domain (not shown here) occur inside the swirl vanes.

As observed in Figure 8 the general observation is that both the mean swirl (U_0), axial (V_0) and radial (W_0) velocities computed using both the Realizable k-ε and LES agreed very well for all the radial locations. There is only a discrepancy in the swirl component at Z = 0.037 m where the LES data predicts a higher peak of mean swirl than the k-ε, nevertheless this difference is only marginal and has no effects in the downstream flow field. The inlet flow is highly inhomogeneous with a high level of anisotropy after the swirler device which is evidenced by the high peaks of mean swirl velocity at z = 0.033 and 0.037 m. The estimated turbulent intensity at Z = 0.033 m is 15%. Furthermore, it can be seen that the radial distribution of the mean axial velocity is clearly not constant, and a highly peaked form appears very close to the outer wall. The phenomena causing this axial profile deflection is not simple. As pointed out by Chigier and Beér (1964) the maximum axial velocity profile occurs close to the outer wall only when an outlet effect is presented, in the present case it comes from the convergent nozzle (the conical shape of the bluff-body) at the annulus channel exit. It again reinforces the necessity of running full domain simulations and treating the problem properly in order to capture such phenomena. The full domain simulations allow this analysis whereas for instance

a decomposition of domain involving only a short cylindrical section would have hidden such phenomena.

From Figure 8, the mean swirl velocity profile displays a smooth and constant profile in the centre of the annulus (obviously away from the walls) with a mean velocity about 25 m/s. The downstream convergent nozzle has little influence on the form of the swirl profile distribution as also confirmed in Chigier and Beér (1964). The radial profile of mean radial velocity is quite smooth with a minimum of -2 m/s in the centre of the annulus which represents less than 10% of the maximum velocity computed from the other two velocity components. In summary, both the k-ε and LES results are almost identical inside the annulus and no significant discrepancy involving the three components of the velocity is observed. This demonstrates that the Realizable k-ε model can accurately predict inflow conditions involving through-the-vane computations.

Figure 7. Flow through-the-vane showing the mean swirl and axial velocity components through the annulus channel and swirl device. The inlet probe line is placed after the swirl device.

Figure 8. Inlet boundary conditions generated at y = - 0.0341m upstream the bluff-body exit from the full domain burner computations. Indication A (at Z = 0.029 m) is located at the inner wall of the annulus channel and B (at Z = 0.0377 m) is located at the outer wall of the annulus. The probe line where data is collected is indicated in Figure 7.

Finally, the degree of swirl has to be determined. The swirl number (S_N) is represented by a dimensionless number (equation 27) that represents the ratio between the axial fluxes of angular momentum (G_φ) to the product of the axial flux of linear momentum (G_x) and a characteristic length scale (R) in this case the outer radius of the annulus channel (Beér and Chigier (1972), Gupta et al. (1984) and Sheen et al. (1996)). Since the axial fluxes of linear and angular momentum are conserved through the annulus section the swirl number is also used here as a mean of checking numerical convergence across the domain.

$$S_N = \frac{G_\varphi}{G_x R} = \frac{\int_0^R \mathrm{VU} r^2 dr}{R \int_0^R V^2 r dr} \tag{27}$$

To calculate the swirl number for this study, equation (27) is integrated along the inlet surface area and the calculated swirl number is S_N = 1.32.

B. Mean flow properties

The computations obtained using RANS (k-ε and RSM) and LES are presented for the three mean velocity components (Swirl (U), Axial (V) and Radial (W)). All the turbulence models were run on the fine mesh as studied in section III.C. The assessment is carried out qualitatively and quantitatively hence providing valuable information on how well each model reproduced the complex flow generated by the highly swirling

motion. For each model at different measurement points a direct comparison is presented and correlated with the flow phenomena presented in that specific region.

It can be observed in Figure 9 that all the turbulence models applied were capable of correctly predicting the flow symmetry behaviour of the axial profile in the radial direction. Velocity plots are relevant for the position until y = 38 mm which is the area where the central recirculation zone forms and reaction takes place (Cavaliere 2013a,b)), nevertheless experimental data beyond this point is available for the mean axial velocity component and is plotted here for the purpose of enhancing our numerical validation and completeness of flow physics analysis. Overall the k-ε model tends to overestimate the peaks of velocity in the shear layer zone. The results involving the RSM and LES models are nearly indistinguishable until y = 8mm and some small discrepancies are observed close to the outlet. Figure 9 and Figure 10 (c) also show that low and negative mean axial velocities in the axial directions are presented in the whole burner domain indicating that the internal reversal flow generated due to the swirl component can be found up to the outlet. The length of the CRZ which is higher than the last measurement point (at y = 117 mm) and width of the recirculation zone which extends almost close to the outlet boundary are well-predicted by all the turbulence models used and later on also confirmed by the rms of the axial velocity fluctuations LES (Figure 13). The recirculation zone at y = 8 mm has a width approximately $1.2D_b$ and at y = 80 mm it widens to approximately $2.2D_b$. It also shows that the choice of outlet boundary condition as well as the length of the burner allowed the development of the central recirculation zone without deteriorating the flow field patterns inside the burner.

The peak of velocity values shifts towards the wall as the flow moves downstream towards the outlet. It initially happens because the airstream experiences a strong streamline curvature following the conical geometry in Figure 10 (c) (about 50° which was also observed in the experiments), however the peak intensities gradually decay in the streamwise direction. The maximum peak of mean axial velocities (approximately $1.2U_b$) occurring in the shear layer at y = 8 mm (Figure 9) are well-resolved and an excellent agreement with experiments (within the experimental error of 3%) shows that the area of intense shear layer can be captured using the RSM and LES models for all the axial locations; only minor differences are found at stations y = 80 mm and 117 mm where the LES model performed better than the RANS counterparts. A minimum velocity of approximately -5 m/s occurs at y = 38 mm in the centre of the recirculation zone. As the flow progresses towards the outlet ($y > 1.52D_b$) the shear layer tends to disappear and the velocity drops to less than 7.5 m/s, the width of the CRZ in the outward directions increases as well as the negative velocity in the central recirculation zone.

Figure 9. The predicted radial profile of mean axial velocity for RANS and LES models.

(a) **(b)** **(c)**

Figure 10. Mean velocity profiles: Swirl (a), Radial (b) and Axial (c) contours computed using the RSM turbulence modelling. Horizontal dashed lines represent

measurements stations. The solid black lines on (c) denote zero axial velocity iso-lines (stagnant flow).

The mean swirl and radial velocities profiles are reported in Figure 11 (a) and (b) for both RANS (RSM and k-ε) and LES models. The swirl velocity as shown in Figure 11 (a) reveals that at y = 8 mm and 13 mm in the transition area of the shear layer (0.5 < Z/D_b < 1.25) between the corner rotating flow and the CRZ, the RSM model accurately computes the high gradient of velocities as showed in the experimental data and also shown in Figure 10 (a) while at y = 13 mm in the shear layer the LES results are only qualitatively good. In general the RSM model fails to capture the peaks of velocity which are slightly lower at locations close to the bluff body; this might be related to limitations in the computation of the energy dissipation in the Reynolds-stress modelling (Pope (2000) and Gibson and Launder (1978)). The peak of swirl velocity (approximately 1.05U_b) occurred at the first measurement station (at y = 8 mm), since it is almost 85% of the maximum axial velocity for the same location it confirms how intense the anisotropy is in this region. At y = 33 mm the swirl velocity quickly decays with values remaining between ±3.75m/s. Generally, the k-ε performs poorly in capturing the velocity profile in the shear layer (between 1 < Z/D_b < 2); an overestimation of the velocity (up to 375%) with respect to the experimental value was found.

(a) **(b)**

Figure 11. Columm (a) is the computed radial profile of mean swirl velocity and (b) the computed mean radial velocity for RANS and LES models.

As shown in Figure 11 (b) the radial velocity profile peaks at approximately ± 10 m/s at y = 8 mm, this value which is found in the shear layer represents about 57% of the peak of axial velocity for the same location, therefore the influence of radial velocity in the general flow physics has to be accounted for. This peak was captured by the three turbulence models applied. A general observation is that both LES and RSM data are nearly indistinguishable from the measured data on locations y = 18 and 33 mm where good agreement against experimental data is presented for the CRZ (-1 < Z/D_b < 1) and the high-gradient regions around the peaks of velocity. In terms of maximum velocity prediction both models also behave quite similarly.
The only significant discrepancy between the models is observed at location y = 8 mm. The flow presents a surprising feature in the radial location (1 < Z/D_b < 2) where a set of measurements points indicates that the Radial velocity is negative. It is noticed that the RANS (k-ε and RSM) models give unrealistic predictions before decaying to zero velocity values at the wall. We have also observed that the mean LES data in Zhang (2015) showed the same issues as revealed by our RANS data at y = 8 mm, however no explanation was presented on the possible causes of this mismatching. In contrast, our present LES data suggest that this feature is presented on both sides of the burner and good agreement with the experimental data is achieved evidencing good symmetry and accuracy.

At locations y = 18 and 33 mm the k-ε model tends to over-predict the peak of experimental velocity values by up to 30%. At y = 8 mm the model shows an unrealistic negative velocity in the interval (-2.0 < Z/D_b < -1) covering the corner vortex since the

expected value would be positive. Despite the issues at y = 8 mm a good agreement can still be observed in the high-gradient region of the shear layer ($1 < Z/D_b < 2$); however such tendency is not repeated in the position y = 33 mm because the radial profile is slightly shifted towards the lateral wall. Generally, we can consider that the k-ε model is capable of delivering representative qualitative data.

C. Instantaneous velocity field

Despite the smooth and continuous mean flow fields revealed in Figure 10 using the steady-state RSM, what we can initially observe from the instantaneous snapshot of the velocity field components (Figure 12 (a), (b) and (c)) is that the flow is more complex, with the formation of several irregular roll-up eddies, and asymmetry due to the high velocity fluctuations formed mainly in the shear layer zone. However, we can still observe some important flow features such as the formation of a central recirculation zone (CRZ) in the area of low and negative axial velocity, the increase of the axial velocity due to the sudden expansion of the flow, as well as the corner rotating vortexes. The root mean square (rms) of the three velocity fluctuation components presented in Figure 13 and Figure 14 (a) and (b) are used to quantify the turbulent behaviour by comparison against the experimental data. In order to reinforce the reliability of the present analysis, we have also made direct comparisons with previously reported LES data from Zhang (2015).

(a) **(b)** **(c)**

Figure 12. Instantaneous velocity field countours for (a) Swirl, (b) Radial and (c) Axial.

By contrasting the peak of both the rms fluctuations of the axial (Figure 13) and swirl (Figure 14 (a)) velocity components at the various downstream locations with their respective mean axial (Figure 9) and swirl velocity profiles (Figure 11 (a)) the turbulence intensity and the relative strength of the swirl flow can be explored. At location y = 8 mm it is noticeable that both the mean swirl and axial velocities and its rms have the same magnitude indicating that the flow not only experiences high gradients of velocity in different spatial directions but is also highly turbulent. For the rms of the axial velocity fluctuations, the modelling was capable of computing the magnitude of peak fluctuating velocity at y = 8 mm which is the closest measured location, even though the profile seems to be slightly shifted, symmetry is still preserved. For instance, Figure 13 at location y = 8 mm the maximum fluctuating velocity (≈6.63 m/s) accounts for about 40% of the mean axial velocity for the same location; furthermore at y = 28 mm the axial fluctuating field has the same order of magnitude as the mean field with a fluctuating velocity accounting for more than 85% of the mean axial velocity, therefore demonstrating the high level of turbulence intensity in the reference burner. From Figure 13, at regions close to the inlet at y = 18 mm and 28 mm the numerical results are within the experimental error of 3%, with a smooth velocity profile; this is maintained for locations beyond y = 33 mm, including at y = 38, 80 and 117 mm close to the outlet region even though the velocity profile for the numerical results is less smooth. Overall the flow field is well-captured.

Figure 13. Radial distributions of rms fluctuations of the axial velocity component.

Figure 14 (a) and (b) show the radial profile of the rms of the swirl and radial velocity fluctuations. Overall, for both cases the present LES results were both quantitatively and qualitatively consistent with the measured fluctuating field and the general observation is that symmetry is well captured. Comparing with the mean swirl velocity (Figure 11 (a)) for the location y = 8 mm it can be seen that the peak of fluctuating velocity field is about 50% of the peak of mean, revealing the high turbulence intensity in the azimuthal direction, the maximum values naturally arise in the areas with the largest gradient in the mean swirl velocity; these characteristics are also presented at the location y = 13 mm; however at y = 33 mm the swirl rms level is remarkably high in the recirculation zone with the same magnitude as in the mean field (Figure 11(a)). Similar trends are qualitatively followed by the rms of the radial velocity fluctuations field component (Figure 14 (b)) for which a disagreement with experiments in terms of maximum locus occurs; for the location y = 8 mm the experimental data is not symmetric which makes it difficult to contrast; at y = 18 mm even though there is an under predication of the peak rms, the profile in the central recirculation zone (-1 < Z/D_b < 1) is well-resolved; at the location y = 33 mm the experimental profile is replicated by the numerical simulation.

(a) **(b)**

Figure 14. Columm (a) is the radial distributions of rms fluctuations of swirl and (b) radial velocity components. LES data is also compared with the LES studies of Zhang (2015).

In summary, a number of qualitative similarities with the LES (green lines) from Zhang (2015) is achieved, nevertheless by looking at the green lines in Figure 14 it is noticeable that both the locations and intensities of the peaks of swirl and radial rms computed in Zhang (2015) are smaller and slightly shifted compared to experimental data, such underestimations have been claimed to be associated with insufficient mesh resolution. Regarding the significant underestimation of the rms axial velocity fluctuations (green line in Figure 13, especially at locations y = 8 mm, 13 mm and 23 mm), Zhang (2015) attributed these to a lack of turbulence inflow information for the inlet boundary condition in the LES model. The improved computed rms data from the present studies presented herein are fundamentally associated with the numerical methodology adopted for the inlet boundary condition generation as well as the good mesh resolution in the shear flow for LES which was discussed in section III-G. Finally, at some locations (i.e. at y = 33 mm) the rms of the swirl velocity fluctuations displayed a fairly asymmetric behaviour considering the two LES cases; nonetheless this same behaviour also appears in the experimental data.

D. Turbulent kinetic energy analysis

The turbulent kinetic energy is assessed and validated for both RANS (k-ε and RSM) and LES models. The characteristic turbulent velocity which is proportional to the turbulent kinetic energy is computed by taking the square-root of the turbulent kinetic energy as suggested in Cavaliere (2013a), thus:

$$q = \sqrt{\frac{(u_{rms}{}^2 + v_{rms}{}^2 + w_{rms}{}^2)}{2}} \quad (28)$$

In order to allow a direct comparison between the RANS and LES models with the experimental data, the expression in equation (28) is divided by the bulk velocity (U_b) to generate a dimensionless term which is essentially the turbulent kinetic energy (Cavaliere (2013a)). Overall, there is a qualitative agreement between the numerical simulations and the experimental data covering the radial direction ($-1.5 < Z/D_b < 2.0$) as shown in Figure 15 and Figure 16. In Figure 15 at the first measurement station (y = 8 mm) the two distinct peaks of turbulence in the strong shear layer zone ($\pm 0.5 < Z/D_b < \pm 1.0$) and in the CRZ zone ($-0.5 < Z/D_b < 0.5$) were quantitatively predicted using LES with values within the experimental error of 3% showing the maximum turbulent kinetic energy followed by a steep gradient across the outer shear layer towards the lateral walls. The shear layer zone is characterized by a strong value of (q) that increases until it reaches a maximum peak at station y = 13 mm. At this station (q) accounts for more than 60% of the characteristic velocity related to the bulk velocity; a high level of anisotropy is present due to the high gradient of velocity values across this region. As pointed out in the experiments of Cavaliere (2013a), Schefer et al. (1987) and Jones and Wilhelmi (1989) the maximum level of turbulence in a swirl combustion chamber is established at the outer and inner shear layers formed between the central recirculation zone and the corner rotating vortexes.

Both RANS models over predict the turbulent kinetic energy by approximately 53% in the centre of the combustion chamber ($-0.5 < Z/D_b < 0.5$), whilst at the low valley in between the two-peaks (at $0.5 < Z/D_b < 1$) the k-ε under-prediction is about 354% lower than the experimental value. These can have implications if used in a practical combustion chamber, as the turbulence intensity in this area of the combustion chamber influences spray break-up processes and droplets evaporation. At y = 33 mm the RSM model followed the same qualitative trends as the LES data whilst the k-ε presented a rather small peak of q ($\approx$ 35% of U_b) as well as a reasonable prediction in the level of the (q) in the recirculation zone ($-1 < Z/D_b < 1.0$). The RSM and LES models (Figure 16 (a) and (c)) show that the maximum turbulent kinetic energy occurs at the both the inner and outer side of the conical shear layer due to intense interactions between the issuing gas and the almost stagnated flow in the central recirculation zone and the corner vortexes.

Figure 15. Comparison of the characteristic turbulent velocity (q) between k-ε, RSM and LES models. The red block *symbols* refer to the experimental validation data.

Figure 16 (a) shows that the LES mean TKE is observed to be high (100 J/kg) in the shear layer zones and peak values of $\approx$ 212 J/kg are found at the edges of the annulus and bluff-body under $y \leq 33$ mm, which is in the CRZ. As the flow progresses towards the outlet, turbulent kinetic energy is gradually dissipated. In Figure 16 (a) the increase in TKE from the sudden expanded flow driven by the contraction conical surface is due to the strong shear flow interaction between the CRZ and CRV zones as also presented in Figure 10 (c). The flow expands at the bottom wall corners of the combustion chamber, greatly increasing the levels of turbulent kinetic energy at the bluff-body corner. From $8 \leq y \leq 13$ mm an increase in turbulent kinetic energy activity is noticed

and this relates to Figure 15 where the peak of TKE at y = 13 mm is approximately 23% higher than at y = 8 mm.

For most of the downstream positions $y >$ 33 mm in Figure 16 (a), (b) and (c), the radial motion has already impinged on the wall and lost energy due to viscous dissipation. The low velocity profile at the CRV of the combustor chamber (as observed in Figure 10 (c)) also aids the deceleration of the flow in that area, delaying the dissipation of energy close to the corners. One of the immediate effects of confining the flow can be associated with the high turbulent kinetic energy flow generated in the shear layer that quickly impinges on the wall and as a consequence of the viscous boundary layer interaction this energy is rapidly dissipated by the viscous friction with the wall. Flow with sufficient energy keeps moving in the streamwise direction with a gradual decrease in mean streamwise and radial velocities. It is worth mentioning that for downstream locations in the range 8 < y < 13 mm there is an intense production of turbulent kinetic energy which is largely generated in the region of shear layer interactions. These interactions appear in all spatial locations as can be seen by the rms fluctuations of swirl, axial and radial velocity components (as observed in Figures 13 and 14 (a) and (b) at y = 8 and 13 mm) which have the same magnitude.

(a) **(b)** **(c)**

Figure 16. Mean of turbulent kinetic energy (TKE) scalar field representation at the symmetric mid-plane for (a) LES, (b) k-ε and (c) RSM models. Horizontal dashed lines indicate downstream directions as discussed in the text (y = 8, 13, 33 and 75 mm).

E. Anisotropy assessment of strong swirling flow

In Figure 17 the Lumley triangle is presented considering the data collection at four different axial stations inside the combustion chamber. The Reynolds-stress values are obtained from the RSM simulations. Data points are collected in the radial direction from the centre of the combustor line starting from 'a' at (x, y, z) = (0, y, 0) mm to 'c' (x, y, z) = (0, y, 47.4) mm; where $y = [8, 28, 80, 117]$ mm is a vector with the four axial stations. For each axial station 1000 probing points are equally spaced from 'a' to 'c' the Reynolds stresses are collected for each point and used to generate the anisotropy matrix (b_{ij}) using equation (19). Data points are plotted and oriented starting from point 'a' that is located in the middle of the combustion chamber, an intermediate and indicative point 'b' that lies in between the centre of the combustion chamber and point 'c'. As previously discussed in Figure 9, Figure 10, Figure 11, Figure 12, 13 and 14 significant amounts of shear flow interactions occur in a spatial location in between 'a' and 'c' which is the area of flow expansion and interaction between the CRZ and CRV vortexes.

Figure 17. The Lumley triangle on the plane of invariants η (vertical axis) and ξ (horizontal axis) of the Reynolds-stress anisotropy tensor at four different axial locations. The lines and vertices correspond to the states and shapes in see Table 3.

It can be observed in Figure 17 that for all the axial stations the turbulence state is predominantly axisymmetric including the central recirculating zone and the shear layer, especially at stations y = 8 mm and 28 mm. Near to the top of the bluff-body (y = 8 mm) turbulence intensities are higher due to the intense shear layer interaction of the expanding flow (see discussion in section IV-C). An interesting finding is that inside the central recirculation zone, except for location y = 8 mm which is close to the flow expansion, turbulence has a tendency to behave more isotropically which appears to be well substantiated by DNS of confined swirling flows as in Yang et al. (2015) and experiments in swirling pipe as in Pashtrapanska et al. (2006). No evidence of extreme intensities (towards the 1-component turbulence) were found and data analysis evidenced that for the present burner η is often less than 1/6. In general, the turbulence state is very sensitive to variations in the flow spatial location which are usually followed by a change in turbulence state. The Reynolds-stress model applied satisfies strong realisability for the trajectories at the four different axial locations.

As the flow travels downstream (Figure 17 at y = 28 mm), it can be observed that turbulence is essentially axisymmetric with $\xi > 0$ covering one of the limiting states of componentality of the invariant map; the turbulence fluctuations are predominantly in two directions evidencing its multidimensional nature. This state is also known as axisymmetric expansion which has an oblate spheroid shape (see Table 3). Further downstream at y = 80 mm the flow in the centre of the recirculation zone behaves more isotropically resulting in a spherical shape (red and pink circles in Figure 17). It can be substantiated based on the rms data as presented in the LES analysis (Section IV.C) which confirmed that flow velocity fluctuations in all spatial directions at the central recirculation zone have similar magnitudes.

At y = 80 mm (Figure 17) as the probing moves in the outward direction (from 'a' to 'c') towards the combustion chamber wall the flow experiences a rapid change in turbulence state from almost an axisymmetric expansion (oblate spheroid in Table 3) to an axisymmetric contraction (prolate spheroid in Table 3). While crossing the CRZ region a slight increase in anisotropy level occurs suggesting that turbulent fluctuations exist in two directions and necessarily has one negative eigenvalue. These current findings corroborate with those in Radenković et al. (2014) that investigated anisotropy for simple swirling pipe flow. However, this present study extends the understanding for the flow with multiple vortexes and shear layer interactions with strong gradients of velocity mainly in the radial direction (which is not the case in previous studies and in pipe flow situations), furthermore the physics of flow in a confined combustion chamber shows more accentuated interactions in the shear layer, for example, leading to the formation of several vortexes interactions, corner and central recirculation interaction as well as the wake flow (see Figure 10 (c)). At point 'c' turbulence is essentially axisymmetric $\xi < 0$ (prolate spheroid; Table 3) with a slight preference towards the two-component boundaries.

At distance y = 117 mm the anisotropy at the centre of the burner is shifted from the left-hand to the right-hand presenting a less isotropic behaviour compared with the data at y = 80 mm. This gradual increase in anisotropy towards the two-component state is the result of the flow becoming more developed with a decayed level of swirl towards the outlet. The remaining data is within the map and far away from the boundaries (i.e. the black circles in the centre of the triangle; Figure 17) and are part of the plane-strain turbulence and has at least one zero eigenvalue.

F. Flow turbulence structure

Even though the experimental measurements for turbulent coherent structures are unavailable, the LES simulations, if validated against experimental data, can be used to carry out further analyses of the swirling turbulence structure. The characteristic angular speed ($\Omega = 1413s^{-1}$) evaluated at the annulus exit is computed based on the peak of swirl velocity entering the combustor and can be used as an indication of the main flow rotation. The iso-surface of vorticity in the streamwise direction is plotted in Figure 18 (a) and (b). This data reveals some interesting turbulent structures encountered in a typical confined strong swirling flow combustion chamber which is not frequently explored in literature.

(a) **(b)**

Figure 18. (a) 2D mid-plane showing the instantaneous snapshot of axial vorticity field and (b) the cross-sections at y = 25 mm and 75 mm structures coloured by the scalar axial vorticity intensity.

A zoom-in of zones A and B in Figure 18 (a) shows for instance that randomly spread, small and elongated worm-like vortices are originated within the central recirculation zone which is surrounded by the conical shear flow and the wake of the bluff-body. These vortices are coloured by the vorticity intensity in the streamwise direction. Zone A is an area of negative streamwise velocity surrounded by high intensity of swirl and radial fluctuating velocities. These vortices coloured in yellow rotate with a frequency about 10 times higher than the characteristic angular speed and they are generated due to the interactions between the fluctuating field and the mean velocity in the inner zone of the shear flow as in Figure 18 (b) for the cross-section plane at y = 25 mm.

Further downstream above y = 75 mm it is observed from the rim of the bluff-body that the decay of the turbulent kinetic energy is almost complete (refer to Figure 16 (a)) therefore in zone B the vortices are shaped as large-columnar clusters. The radial profile of both swirl and radial velocities in this area are very small compared to the values at the first measurement station, at y = 8 mm (see Figures 10 (a) and (b), and 11 (a) and (b)), hence these vortices are particularly driven by the axial velocity.
The visualisation of the instantaneous 3D vorticity (Figure 19) allows the qualitative assessment of the formation of distinct vorticities in the confined swirling flow. The iso-surface of the vorticity is plotted for a frequency which is one order of magnitude larger than the characteristic bulk angular speed. In Figure 19 this analysis is paramount for future studies of complex reacting flow involving flame ignition and instabilities such as local and global extinction, the latter is related to a significant increase in inlet velocity that changes the frequency of the vortices.

Figure 19. Instantaneous iso-surfaces of coherent 3D vorticity structures with the symmetric plane indicating the contours of mean axial, radial and swirl velocities.

Compact large ring-type structures (indicated by red arrows in Figure 19) next to the top of the bluff-body were identified by the swirl and radial vorticity iso-surfaces and they can be considered as a manifestation of the precessing vortex core motion mainly

on the boundary of the low velocity recirculation zone. This vortex motion is driven by the main swirl velocity which rotates the central vortex around the axis of symmetry. It can be deduced from the swirl and radial iso-surfaces that the vortices have two clearly distinct large topological structures (a primary and a secondary ring) whereas these cannot be similarly deduced from just the axial profile. In the central recirculation zone (CRZ) (Figure 19, axial velocity) for the iso-surface of 3D coherent vorticity there are small and random vorticity structures formed and they are caused by the high swirl number and strong shear interaction, as also observed in Coats (1996), García-Villalba (2006) and Cheng et al. (2010). It can be concluded from Figure 10 (a), (b) and (c) that the influence of the conical bluff-body not only changes and increases the flow velocity in the vicinity of the bluff-body annulus exhaust but also has an important contribution in increasing the turbulence kinetic energy (Figure 16), however it is not conclusive whether the bluff-body conical shape has a substantial influence on the formation of vortices and how it might act in the transition from small worm-shape to large-columnar vortices (Figure 18 and 19).

V. CONCLUDING REMARKS

We examined the highly swirling and confined bluff body flow typically encountered in a swirl stabilised burner relevant for the studies of gas-turbine combustion. RANS and LES techniques were used to simulate the turbulent flow through the combustion chamber. The main features of the swirling flow such as the types of vortexes, recirculation zones, the turbulence intensity in the shear flow, as well as the high anisotropy of the flow and coherent structures were captured and compared with experimental and reported LES data. We found that whilst there is qualitative agreement between the computed RANS data, experimental and reported LES data for the characteristic turbulent velocity profiles, differences exist elsewhere. For the RANS k-ε method, the peak gradients of the turbulent kinetic energy within the shear layer are underpredicted by up to 354%, whereas for the RSM method, the turbulent kinetic energy values in the central recirculating zone just downstream of the injection are underpredicted by up to 53%.

However, the accurate predictions of the contributions of the swirl flow motion to the central recirculating zone is important because it affects the flame stability in the combustion chamber. Atypically, by carrying out a whole domain RANS simulation, we have included the contribution of the swirl device to the inlet flow conditions that in turn affect the central recirculating zone. To reduce the computational price of solving the full domain including the swirl device with the LES method, the velocity and Reynolds-stress data from full-domain RANS simulations were mapped and used to initialise LES inflow boundary conditions. We also assessed the Dynamic Smagorinsky model but found no substantial improvements in mean flow velocity predications compared to the original Smagorinsky model for the experimental conditions that we considered. A carefully considered mesh capable of solving 95.6% of the turbulence resolved energy was also constructed. The LES method presented predictions of the turbulent fluctuation fields in the azimuthal, radial and axial directions, for both the spatial locations and the intensity of the peaks mostly within the

experimental error (3%) values; a better resolution than in currently reported LES data and this is important for prospective turbulent spray combustion simulations. The Lumley-invariant map was constructed and used to visualize the highly anisotropy flow and assess the Reynolds-stress in the central recirculating zone and shear layer; hitherto this has been applied only to pipe flows. The assessments indicate the presence of a mostly isotropically shaped turbulent flow in the centre of the central toroidal recirculating zone, whilst in the shear layer, the flow is two-component and axisymmetric. These are important in practical applications for the siting of ignitors in the chamber and understanding the influence of combustion in the anisotropy state. The flow turbulence structures indicated a high vorticity region at the central recirculation zone which is characterised by a negative streamwise velocity surrounded by highly intense swirl and radial fluctuating velocities; these decay further away from the zone, downstream of the combustor, however. Thus, at the central recirculation zone, flow is reversed towards the top and walls of the combustor. This explains why, in reacting flows in swirl-stabilised burners, the flame stability is improved; the recirculating flow carries warmer flows to the base of the flame. These results denote the appropriateness of the methods used for this study.

Acknowledgements: This work has been financially supported by the Centre for Fluid and Complex Systems at Coventry University, and partly by the UGC-UKIERI 2016-17-050 grant. The first author is grateful to Dr Andrea Giusti from Cambridge University for discussions on numerical modelling. We also thank Dr Paulo Beck from DLR-Germany for help with the invariant map, and Dr Kuppuraj Rajamanickam from IISc-Bangalore for discussions on the physics of swirling flows.

Bibliography

Abujelala, M., Jackson, T., and Lilley, D. (1984) 'Swirl Flow Turbulence Modeling'. In 20th Joint Propulsion Conference. Ed by: American Institute of Aeronautics and Astronautics

Beér, J. M. and Chigier, N. A. (1972) Combustion Aerodynamics. London: Applied Science Publishers Ltd.

Benim, A. C., Nahavandi, A., and Syed, K. (2005) 'URANS and LES Analysis of Turbulent Swirling Flows'. Progress in Computational Fluid Dynamics, An International Journal 5 (8), 444-454

Benim A.C., Escudier M.P., Nahavandi A., Nickson A.K., Syed K.J., and Joos F. (2010) 'Experimental and Numerical Investigation of Isothermal Flow in an Idealized Swirl Combustor'. International Journal of Numerical Methods for Heat & Fluid Flow 20 (3), 348-370

Billant, P., Chomaz, J., and Huerre, P. (1998) 'Experimental Study of Vortex Breakdown in Swirling Jets'. Journal of Fluid Mechanics 376, 183-219.

Bonello, B. (2018) Spray Combustion Analyses: Comparison of Turbulence Models. MSc Thesis. Coventry University, United Kingdom.

Bosch, J., Jong, S., Hoefnagels, D., and Slade, D. R. (2017) 'Aviation Biofuels: Strategically Important, Technically Achievable, Tough to Deliver'. *Grantham Institute Briefing Paper no* 23

Cai, J., Fu, Y., Elkady, A., Mongia, H., and Jeng, S. (2003) 'Effect of Confinement Size on Swirler Cup Aerodynamics'. In 41st Aerospace Sciences Meeting and Exhibit. ed.: American Institute of Aeronautics and Astronautics

Cavaliere, D. E. (2013a) Blow-Off in Gas Turbine Combustors. PhD thesis: University of Cambridge

Cavaliere, D. E., Kariuki, J., and Mastorakos, E. (2013b) 'A Comparison of the Blow-Off Behaviour of Swirl-Stabilized Premixed, Non-Premixed and Spray Flames'. Flow, Turbulence and Combustion 91 (2), 347-372

Cheng, M., Lou, J., and Lim, T. T. (2010) 'Vortex Ring with Swirl: A Numerical Study'. Physics of Fluids 22 (9), 097101

Choi, J., Jung, E., Kang, S., and Do, H. (2018) 'Modeling Swirl Decay Rate of Turbulent Flows in Annular Swirl Injectors'. AIAA Journal 56 (12), 4910-4926

Chigier, N. A. and Beér, J. M. (1964) 'The Flow Region Near the Nozzle in Double Concentric Jets'. Journal of Basic Engineering 86 (4), 797-804

Coats, C. M. (1996) Coherent Structures in Combustion. Progress in Energy and Combustion Science, 1996, 22, 5, 427-509

Deardorff, J. W. (1970) 'A Numerical Study of Three-Dimensional Turbulent Channel Flow at Large Reynolds Numbers'. Journal of Fluid Mechanics 41 (2), 453-480.

Denaro, F. M. (2011) What does Finite Volume-Based Implicit Filtering Really Resolve in Large-Eddy Simulations? Journal of Computational Physics, 2011, 230, 10, 3849-3883

Erlebacher, G., Hussaini, M. Y., Speziale, C. G., and Zang, T. A. (1992) 'Toward the Large-Eddy Simulation of Compressible Turbulent Flows'. Journal of Fluid Mechanics 238, 155-185.

Emory, M. and Iaccarino, G. (2014) 'Visualizing Turbulence Anisotropy in the Spatial Domain with Componentality Contours'. Cent.Turbul.Res.Annu.Res.Briefs, 123-138

Escue, A. and Cui, J. (2010) 'Comparison of Turbulence Models in Simulating Swirling Pipe Flows'. Applied Mathematical Modelling 34 (10), 2840-2849

Freitag, M. and Klein, M. (2005) 'Direct Numerical Simulation of a Recirculating, Swirling Flow'. Flow, Turbulence and Combustion 75 (1), 51-66

García-Villalba, M., Fröhlich, J., and Rodi, W. (2006) 'Identification and Analysis of Coherent Structures in the Near Field of a Turbulent Unconfined Annular Swirling Jet using Large Eddy Simulation'. Physics of Fluids 18 (5), 055103

Germano, M., Piomelli, U., Moin, P., and Cabot, W. H. (1991) 'A Dynamic subgrid-scale Eddy Viscosity Model'. Physics of Fluids A: Fluid Dynamics 3 (7), 1760-1765

Gibson, M. M. and Launder, B. E. (1978) 'Ground Effects on Pressure Fluctuations in the Atmospheric Boundary Layer'. Journal of Fluid Mechanics 86 (3), 491-511.

Gilchrist, R. and Naughton, J. (2003) 'An Experimental Study of Swirling Jets with Different Initial Swirl Profiles'. In 41st Aerospace Sciences Meeting and Exhibit. Ed.: American Institute of Aeronautics and Astronautics

Giusti, A., Mastorakos, E. (2017). Detailed chemistry LES/CMC simulation of a swirling ethanol spray flame approaching blow-off, P Combust Inst. 36:2 2625-2632.

Giusti, A. (2019) Cambridge swirl spray flame Guide for groups who intend to submit calculations for comparisons. Sixth Workshop on the Turbulent Calculations of Sprays, Santa Cruz de Tenerife, Spain. Available from <http://www.tcs-workshop.org/> [accessed 13 Feb. 2019]

Greitzer, E. M., Tan, C. S., and Graf, M. B. (2007) Internal Flow: Concepts and Applications: Cambridge University Press

Gui, N., Fan, J., Cen, K., and Chen, S. (2010) A Direct Numerical Simulation Study of Coherent Oscillation Effects of Swirling Flows. Fuel, 2010, 89, 12, 3926-3933

Gupta, A. K., Lilley, D. G., and Syred, N. (1984) 'Swirl Flows'. Tunbridge Wells, Kent, England, Abacus Press, 1984, 488 p.

Hsiao, G. and Mongia, H. (2003a) 'Swirl Cup Modeling Part 3: Grid Independent Solution with Different Turbulence Models'. In 41st Aerospace Sciences Meeting and Exhibit. Ed.: American Institute of Aeronautics and Astronautics

Hsiao, G. and Mongia, H. (eds.) (2003b). 'Swirl Cup Modeling Part 2: Inlet Conditions. In 41st Aerospace Sciences Meeting and Exhibit. Ed.: American Institute of Aeronautics and Astronautics

Henkes, R. A. W. M., Van Der Vlugt, F. F., and Hoogendoorn, C. J. (1991) Natural-Convection Flow in a Square Cavity Calculated with Low-Reynolds-Number Turbulence Models. International Journal of Heat and Mass Transfer, 1991, 34, 2, 377-388

IATA, Sustainable Alternative Fuel - Advocacy, 2015. Available from https://www.iata.org/whatwedo/environment/Documents/safa-1st-edition-2015.pdf [accessed 5 Mar. 2019]

ICAO, Sustainable Aviation Fuels Guide, 2017. available from https://www.icao.int/environmental-protection/knowledge-sharing/Docs/Sustainable%20Aviation%20Fuels%20Guide_vf.pdf [accessed 13 Feb. 2019]

Jalalatian, N., Tabejamaat, S., Kashir, B., and EidiAttarZadeh, M. (2019) 'An Experimental Study on the Effect of Swirl Number on Pollutant Formation in Propane Bluff-Body Stabilized Swirl Diffusion Flames'. Physics of Fluids 31 (5), 055105

Jarrin, N., Benhamadouche, S., Laurence, D., and Prosser, R. (2006) A Synthetic-Eddy-Method for Generating Inflow Conditions for Large-Eddy Simulations. International Journal of Heat and Fluid Flow, 2006, 27, 4, 585-593

Jones, W. P. and Launder, B. E. (1972) The Prediction of Laminarization with a Two-Equation Model of Turbulence. International Journal of Heat and Mass Transfer, 1972, 15, 2, 301-314

Jones, W. P. and Wilhelmi, J. (1989) 'Velocity, Temperature and Composition Measurements in a Confined Swirl Driven Recirculating Flow'. Combustion Science and Technology 63 (1-3), 13-31

Johnson, B. and Roback, R. (eds.) (1983) 'Mass and Momentum Turbulent Transport Experiments with Confined Swirling Coaxial Jets. I'. 20th Joint Propulsion Conference.

Kadu, P. A., Sakai, Y., Ito, Y., Iwano, K., Sugino, M., Katagiri, T., and Nagata, K. (2019) Numerical Investigation of Passive Scalar Transport and Mixing in a Turbulent Unconfined Coaxial Swirling Jet. International Journal of Heat and Mass Transfer, 142, 118461

Kevin, M. (2009) 'Large Eddy Simulation Applications in Gas Turbines'. Philosophical Transactions of the Royal Society A: Mathematical, Physical and Engineering Sciences, 2009, 367, 1899, 2827-2838, Royal Society

Khalil, A. E. E., Brooks, J. M., and Gupta, A. K. (2016) Impact of Confinement on Flow field of Swirl Flow Burners. Fuel, 2016, 184, 1-9

Launder, B. E. and Spalding, D. B. (1972) *Mathematical Models of Turbulence*: Academic press

Lefebvre, A. H. (1999) Gas Turbine Combustion. 2nd ed. London: Taylor & Francis

Lefebvre, A. H. and Ballal, D. R. (2010) Gas Turbine Combustion: Alternative Fuels and Emissions. CRC press

Liang, H. and Maxworthy, T. (2005) 'An Experimental Investigation of Swirling Jets'. J. Fluid Mech., 2005, 525, 115-159, Cambridge University Press

Lieuwen, T. C. (2012) Unsteady Combustor Physics. Cambridge; New York: Cambridge University Press

Lien, F. S. and Leschziner, M. A. (1994) Assessment of Turbulence-Transport Models Including Non-Linear Rng Eddy-Viscosity Formulation and Second-Moment Closure for Flow Over a Backward-Facing Step. Computers & Fluids, 1994, 23, 8, 983-1004

Lilly, D. K. (1967) "The Representation of Small-Scale Turbulence in Numerical Simulation Experiments," In: H. H. Goldstine, Ed., Proceedings of IBM Scientific Computing Symposium on Environmental Sciences, Yorktown Heights, New York, pp. 195

Liu, S., Meneveau, C., and Katz, J. (1994) 'On the Properties of Similarity Subgrid-Scale Models as Deduced from Measurements in a Turbulent Jet'. Journal of Fluid Mechanics 275, 83-119.

Lu, X., Wang, S., Sung, H., Hsieh, S., and Yang, V. (2005) 'Large-Eddy Simulations of Turbulent Swirling Flows Injected into a Dump Chamber'. Journal of Fluid Mechanics 527, 171-195.

Lucca-Negro, O. and O'Doherty, T. (2001) Vortex Breakdown: A Review. Progress in Energy and Combustion Science, 2001, 27, 4, 431-481

Lumley, J. L. (1979) 'Computational Modeling of Turbulent Flows in Advances in Applied Mechanics. Ed. by Yih, C: Elsevier, 123-176

Lumley, J. L. and Newman, G. R. (1977) 'The Return to Isotropy of Homogeneous Turbulence'. Journal of Fluid Mechanics 82 (1), 161-178.

Lumley, J. L. (2007). Stochastic tools in turbulence. Courier Corporation.

Matheou, G., Bonanos, A. M., Pantano, C., and Dimotakis, P. E. (2010) 'Large-Eddy Simulation of Mixing in a Recirculating Shear Flow'. Journal of Fluid Mechanics 646, 375-414.

Matheou, G. and Chung, D. (2014) 'Large-Eddy Simulation of Stratified Turbulence. Part II: Application of the Stretched-Vortex Model to the Atmospheric Boundary Layer'. Journal of the Atmospheric Sciences 71 (12), 4439-4460

Mastorakos, E. (2017) Forced Ignition of Turbulent Spray Flames. Proceedings of the Combustion Institute, 2017, 36, 2, 2367-2383.

Marchione, T., Ahmed, S. F., and Mastorakos, E. (2009) Ignition of Turbulent Swirling n-Heptane Spray Flames using Single and Multiple Sparks. Combustion and Flame, 2009, 156, 1, 166-180

Merci, B. and Gutheil, E. (2014) Experiments and Numerical Simulations of Turbulent Combustion of Diluted Sprays: TCS 3: Third International Workshop on Turbulent Spray Combustion: Springer Science & Business Media

Merci, B., Roekaerts, D., and Sadiki, A. (2011) Experiments and Numerical Simulations of Diluted Spray Turbulent Combustion: Springer

Mongia, H., Al-Roub, M., Danis, A., Elliott-Lewis, D., Johnson, A., Vise, S., Jeng, S., McDonell, V., and Samuelsen, G. (2001) 'Swirl cup Modeling. Part 1'. 37th Joint Propulsion Conference and Exhibit.

Moin, P., Squires, K., Cabot, W., and Lee, S. (1991) 'A Dynamic subgrid-scale Model for Compressible Turbulence and Scalar Transport'. Physics of Fluids A: Fluid Dynamics 3 (11), 2746-2757

Paik, J. and Sotiropoulos, F. (2010) Numerical Simulation of Strongly Swirling Turbulent Flows through an Abrupt Expansion. International Journal of Heat and Fluid Flow, 2010, 31, 3, 390-400

Pashtrapanska, M., Jovanovi Ä, J., Lienhart, H., and Durst, F. (2006) 'Turbulence Measurements in a Swirling Pipe Flow'. Experiments in Fluids 41 (5), 813

Pope, S. B. (2000) Turbulent Flows. Cambridge: Cambridge University Press.

Pope, S. B. (2004) 'Ten Questions Concerning the Large-Eddy Simulation of Turbulent Flows'. New Journal of Physics 6, 35-35

Proch, F., Pettit, M. W. A., Ma, T., Rieth, M., & Kempf, A. M. (2015). Investigations on the Effect of Different Subgrid Models on the Quality of LES Results. In Direct and Large-Eddy Simulation IX (pp. 141-147). Springer, Cham.

Pierce, C. and Moin, P. (1998) 'Large Eddy Simulation of a Confined Coaxial Jet with Swirl and Heat Release'. In 29th AIAA Fluid Dynamics Conference. Ed.: American Institute of Aeronautics and Astronautics

Pierce, C. D. and Moin, P. (2001) Progress-Variable Approach for Large-Eddy Simulation of Turbulent Combustion: Stanford University California, USA

Piomelli, U., Moin, P., and Ferziger, J. H. (1988) 'Model Consistency in Large Eddy Simulation of Turbulent Channel Flows'. The Physics of Fluids 31 (7), 1884-1891

Radenković, D. R., Burazer, J. M., and Novković, Đ. M. (2014) 'Anisotropy Analysis of Turbulent Swirl Flow'. FME Transactions 42 (1), 19-25

Rajamanickam, K. and Basu, S. (2017) 'Insights into the Dynamics of spray–swirl Interactions'. Journal of Fluid Mechanics 810, 82-126.

Rocklage-Marliani, G., Schmidts, M., and Vasanta Ram, V. I. (2003) 'Three-Dimensional Laser-Doppler Velocimeter Measurements in Swirling Turbulent Pipe Flow'. Flow, Turbulence and Combustion 70 (1), 43-67

Rodi, W. (1991) 'Experience with Two-Layer Models Combining the k-Epsilon Model with a One-Equation Model Near the Wall'. In 29th Aerospace Sciences Meeting. Ed.: American Institute of Aeronautics and Astronautics

Sarkar, S. and Lakshmanan, B. (1991) 'Application of a Reynolds Stress Turbulence Model to the Compressible Shear Layer'. AIAA Journal 29 (5), 743-749

Santhosh, R. and Basu, S. (2016) Transitions and Blow off of Unconfined Non-Premixed Swirling Flame. Combustion and Flame, 2016, 164, 35-52

Sagaut, P., 1967- (2006) Large Eddy Simulation for Incompressible Flows: An Introduction. 3rd ed.: Springer Berlin

Sánchez, A. L., Urzay, J., and Liñán, A. (2015) The Role of Separation of Scales in the Description of Spray Combustion. Proceedings of the Combustion Institute, 2015, 35, 2, 1549-1577

Schefer, R. W., Namazian, M., and Kelly, J. (1987) 'Velocity Measurements in a Turbulent Nonpremixed Bluff-Body Stabilized Flame'. Combustion Science and Technology 56 (4-6), 101-138

Schneider, C., Dreizler, A., and Janicka, J. (2005) 'Fluid Dynamical Analysis of Atmospheric Reacting and Isothermal Swirling Flows'. Flow, Turbulence and Combustion 74 (1), 103-127

Sheen, H. J., Chen, W. J., Jeng, S. Y., and Huang, T. L. (1996) Correlation of Swirl Number for a Radial-Type Swirl Generator. Experimental Thermal and Fluid Science, 1996, 12, 4, 444-451

Shih, T., Liou, W. W., Shabbir, A., Yang, Z., and Zhu, J. (1995) A New k-ϵ Eddy Viscosity Model for High Reynolds Number Turbulent Flows. Computers & Fluids, 1995, 24, 3, 227-238

Shir, C. C. (1973) 'A Preliminary Numerical Study of Atmospheric Turbulent Flows in the Idealized Planetary Boundary Layer'. Journal of the Atmospheric Sciences 30 (7), 1327-1339

Sommerfeld, M., Ando, A., and Wennerberg, D. (1992) 'Swirling, Particle-Laden Flows through a Pipe Expansion'. Journal of Fluids Engineering 114 (4), 648-656

Smagorinsky, J. (1963) 'General Circulation Experiments with the Primitive Equations'. Monthly Weather Review 91 (3), 99-164

Spalart, P. R. and Rumsey, C. L. (2007) 'Effective Inflow Conditions for Turbulence Models in Aerodynamic Calculations'. AIAA Journal 45 (10), 2544-2553

Spencer, A. J. M. (1971) 'Theory of Invariants'. Continuum Phys. 1, 239-353

Simonsen, A. J. and Krogstad, P. (2005) 'Turbulent Stress Invariant Analysis: Clarification of Existing Terminology'. Physics of Fluids 17 (8), 088103

Siemens (2018) Star-CCM+ v12.04 available from <https://mdx.plm.automation.siemens.com/star-ccm-plus> [accessed 8 June 2017]

Sidey, J. A. M., Giusti, A., Benie, P., Mastorakos, E. (2017) The Swirl Flames Data Repository. available from <http://swirl-flame.eng.cam.ac.uk > [accessed 25 Mar. 2018]

Syred, N. (2006) A Review of Oscillation Mechanisms and the Role of the Precessing Vortex Core (PVC) in Swirl Combustion Systems. Progress in Energy and Combustion Science, 2006, 32, 2, 93-161

Syred, N. and Beér, J. M. (1974) Combustion in Swirling Flows: A Review. Combustion and Flame, 1974, 23, 2, 143-201

Talamantes, G. and Maicke, B. A. (2016) 'Evaluation of CFD Codes for Swirl-Driven Combustors'. In 46th AIAA Fluid Dynamics Conference. Ed. by: American Institute of Aeronautics and Astronautics

Tyliszczak, A., Cavaliere, D. E., and Mastorakos, E. (2014) 'LES/CMC of Blow-Off in a Liquid Fueled Swirl Burner'. Flow, Turbulence and Combustion 92 (1), 237-267

Voke, P. R. (1996) 'Subgrid-Scale Modelling at Low Mesh Reynolds Number'. Theoretical and Computational Fluid Dynamics 8 (2), 131-143

Vreman, B., Geurts, B., and Kuerten, H. (1994) 'Realizability Conditions for the Turbulent Stress Tensor in Large-Eddy Simulation'. Journal of Fluid Mechanics 278, 351-362.

Wang, P., Bai, X. S., Wessman, M., and Klingmann, J. (2004) 'Large Eddy Simulation and Experimental Studies of a Confined Turbulent Swirling Flow'. Physics of Fluids 16 (9), 3306-3324

Wang, S., Yang, V., Hsiao, G., Hsieh, S. Y., & Mongia, H. C. (2007). Large-eddy simulations of gas-turbine swirl injector flow dynamics. Journal of Fluid Mechanics, 583, 99-122.

Weber, R., Visser, B. M., and Boysan, F. (1990) Assessment of Turbulence Modeling for Engineering Prediction of Swirling Vortices in the Near Burner Zone. International Journal of Heat and Fluid Flow, 1990, 11, 3, 225-235

Wegner, B., Maltsev, A., Schneider, C., Sadiki, A., Dreizler, A., and Janicka, J. (2004) 'Assessment of Unsteady RANS in Predicting Swirl Flow Instability Based on LES and Experiments'. International Journal of Heat and Fluid Flow 25 (3), 528-536

Wolfshtein, M. (1969) The Velocity and Temperature Distribution in One-Dimensional Flow with Turbulence Augmentation and Pressure Gradient. International Journal of Heat and Mass Transfer, 1969, 12, 3, 301-318

Xia, J. L., Smith, B. L., Benim, A. C., Schmidli, J., and Yadigaroglu, G. (1997) Effect of Inlet and Outlet Boundary Conditions on Swirling Flows. Computers & Fluids, 1997, 26, 8, 811-823

Xu, W., Gui, N., Ge, L., and Yan, J. (2014) Direct Numerical Simulation of Twin Swirling Flow Jets: Effect of Vortex-Vortex Interaction on Turbulence Modification. Journal of Computational Engineering, 2014, 2014, 14

Yang, X., Gui, N., Xie, G., Yan, J., Tu, J., and Jiang, S. (2015) Anisotropic Characteristics of Turbulence Dissipation in Swirling Flow: A Direct Numerical Simulation Study. Advances in Mathematical Physics, 2015, 2015, 9

Zhang, H. (2015) Extinction in Turbulent Swirling Non-Premixed Flames. PhD thesis: University of Cambridge

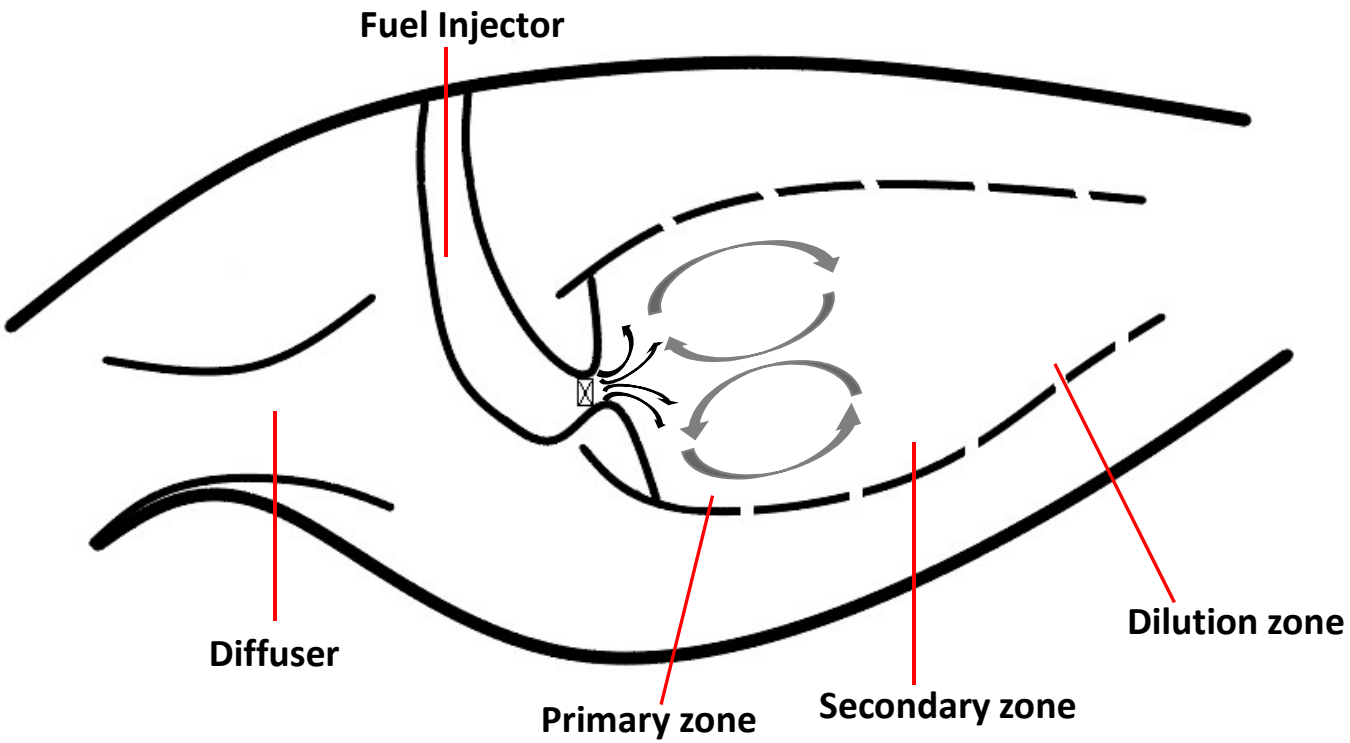
Fuel Injector
Diffuser
Primary zone
Secondary zone
Dilution zone

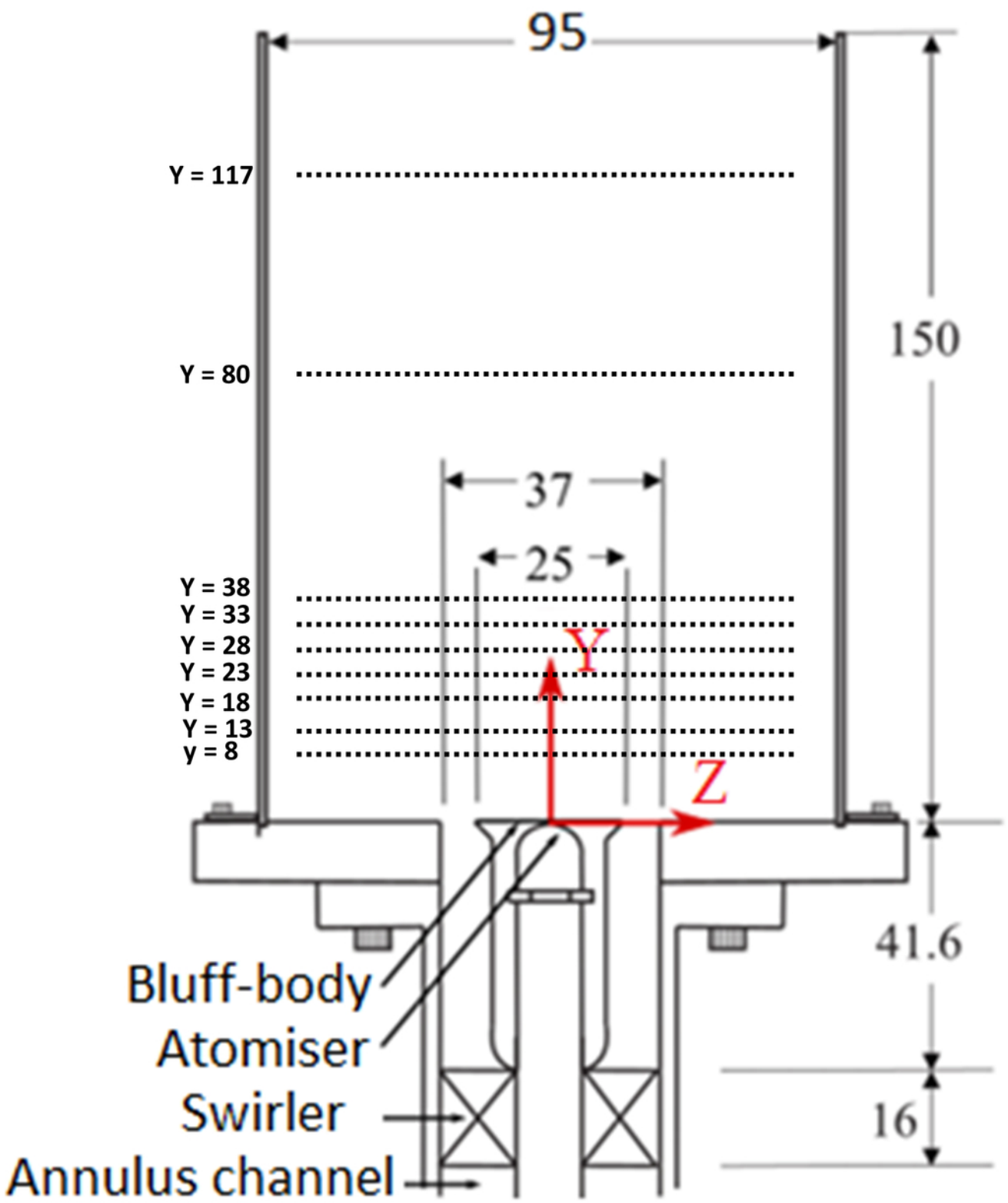
95
150
Y = 117
Y = 80
37
25
Y = 38
Y = 33
Y = 28
Y = 23
Y = 18
Y = 13
y = 8
Y
Z
41.6
16
Bluff-body
Atomiser
Swirler
Annulus channel

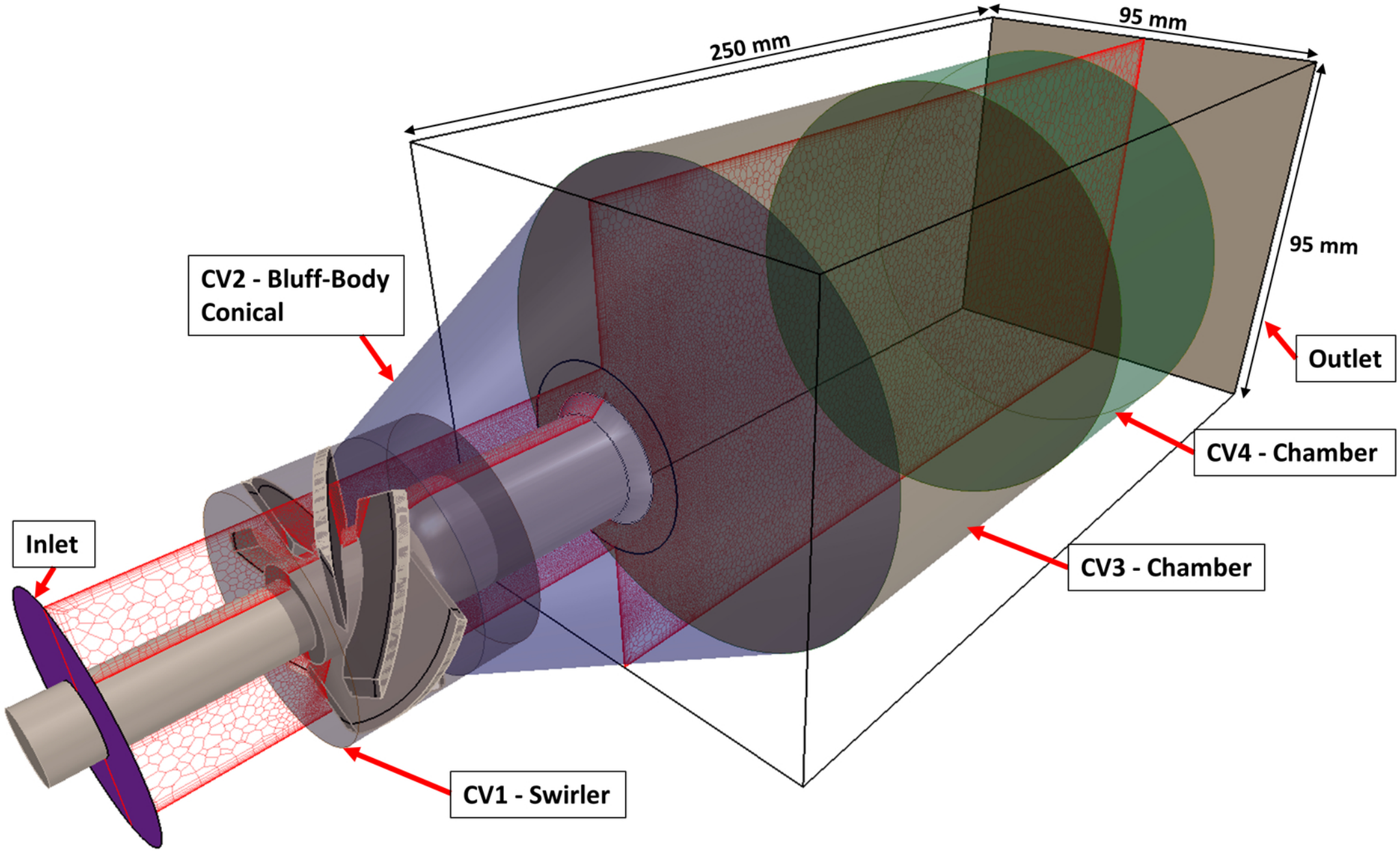
250 mm
95 mm
95 mm
CV2 - Bluff-Body Conical
Outlet
CV4 - Chamber
Inlet
CV3 - Chamber
CV1 - Swirler

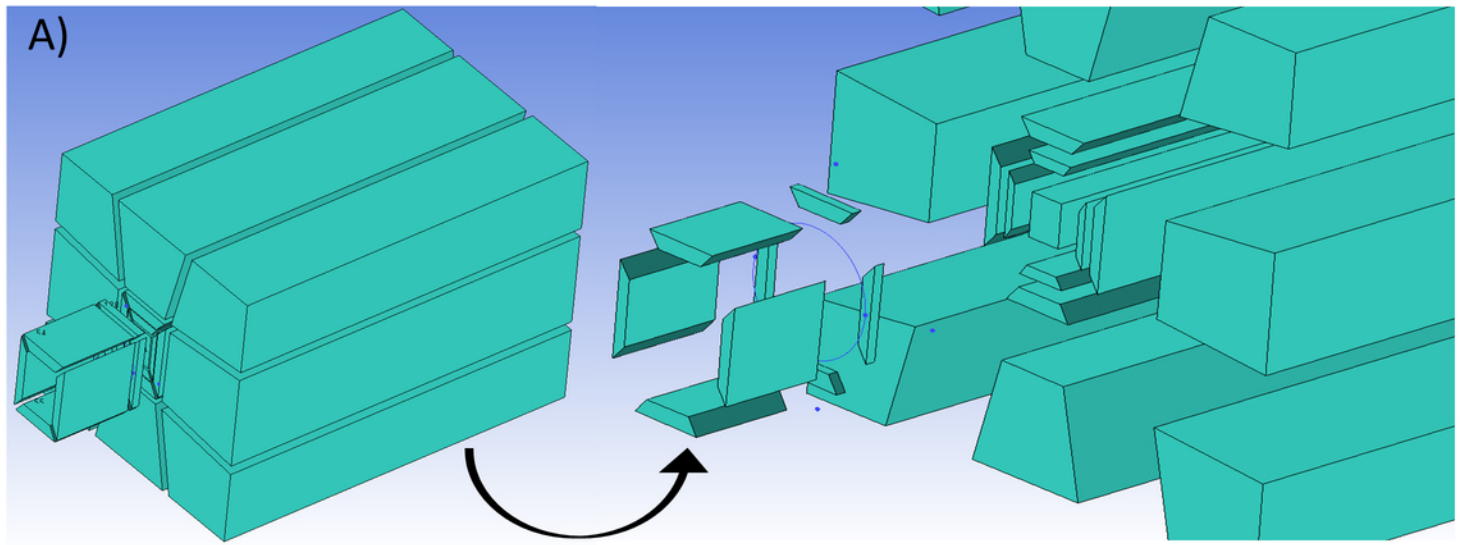
A)

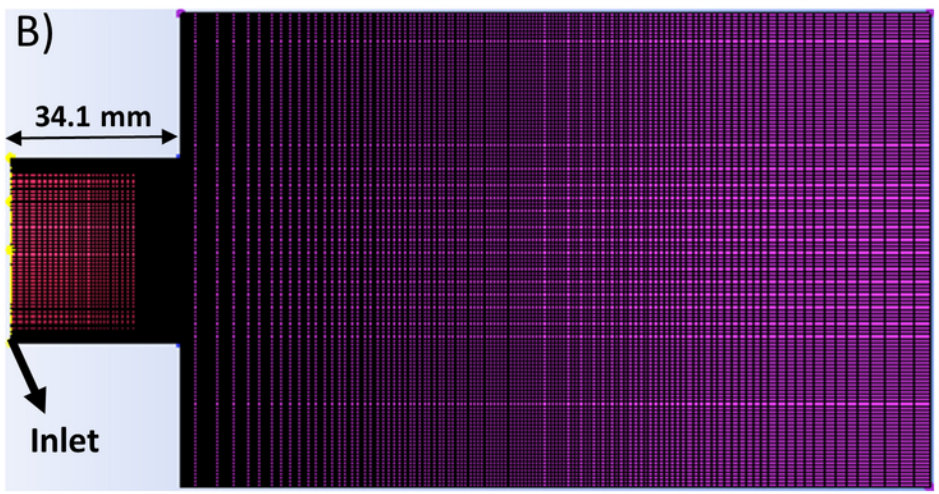
B)
34.1 mm
Inlet

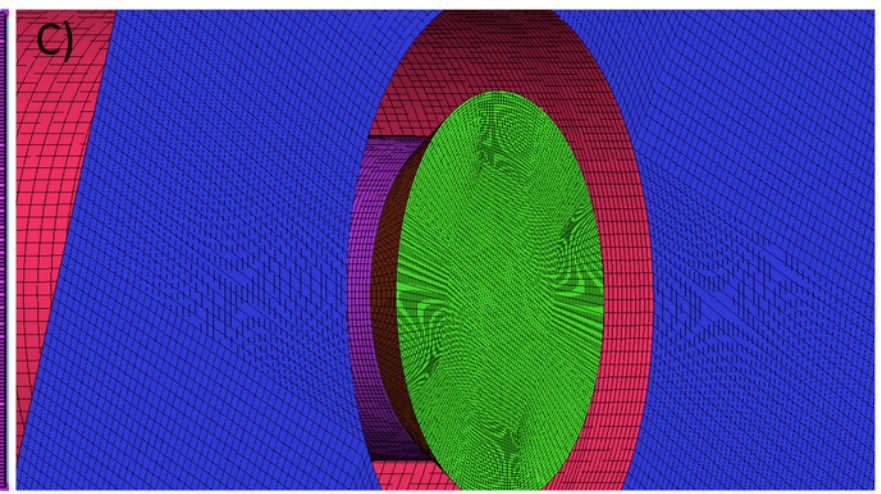
C)

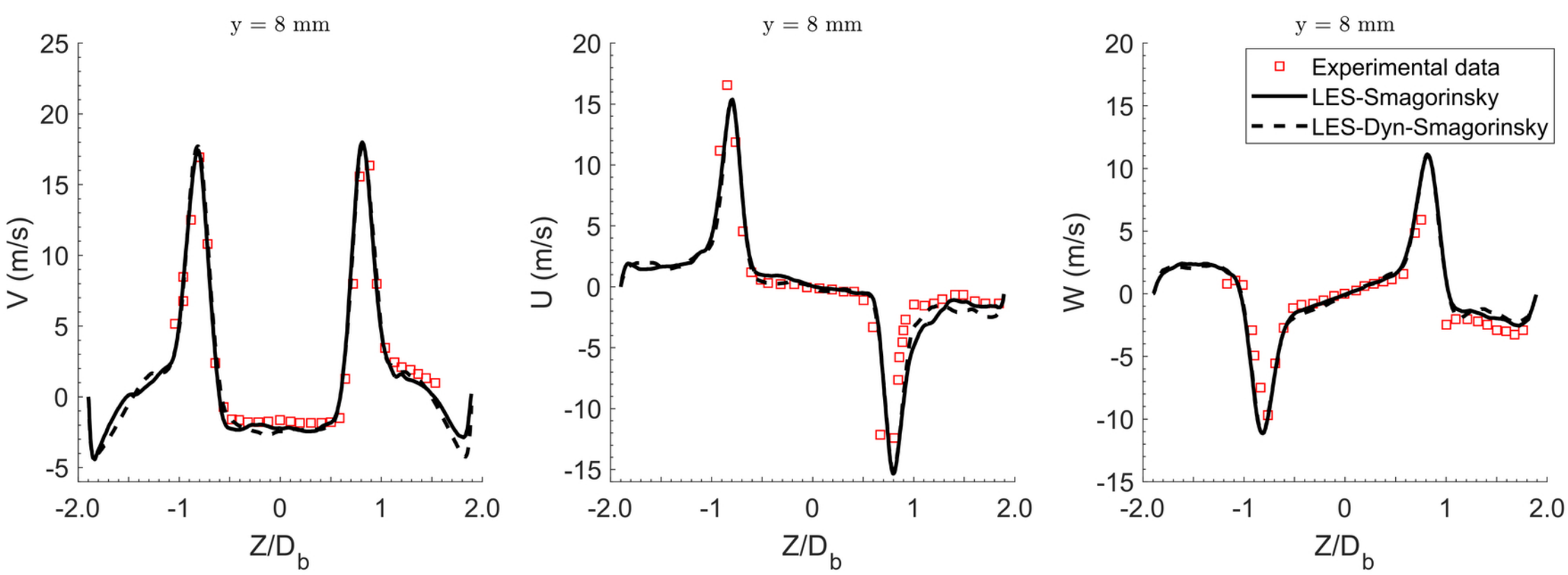
y = 8 mm
V (m/s)
Z/D_b
y = 8 mm
U (m/s)
Z/D_b
y = 8 mm
W (m/s)
Z/D_b
Experimental data
LES-Smagorinsky
LES-Dyn-Smagorinsky

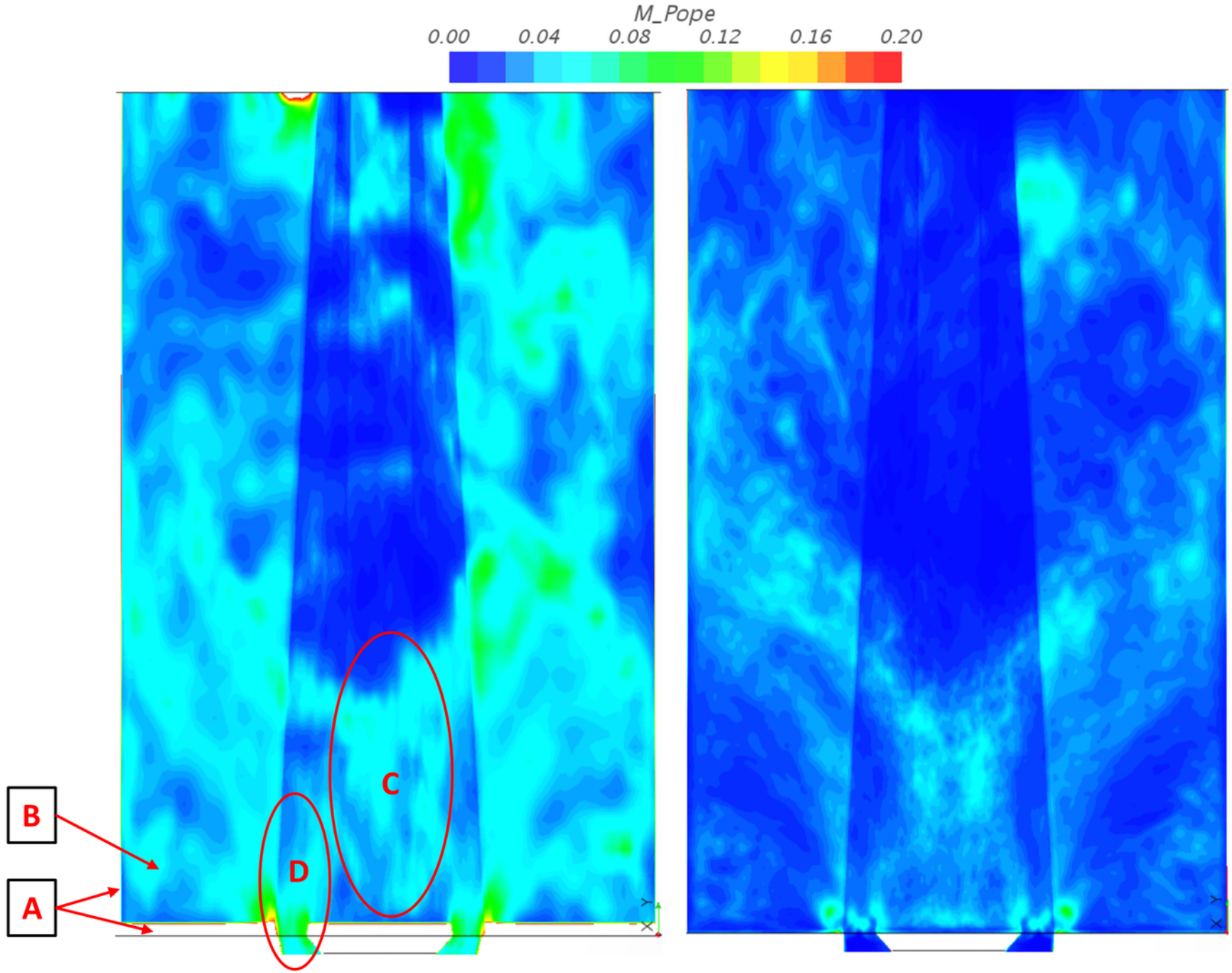
M_Pope
0.00
0.04
0.08
0.12
0.16
0.20
B
A
C
D

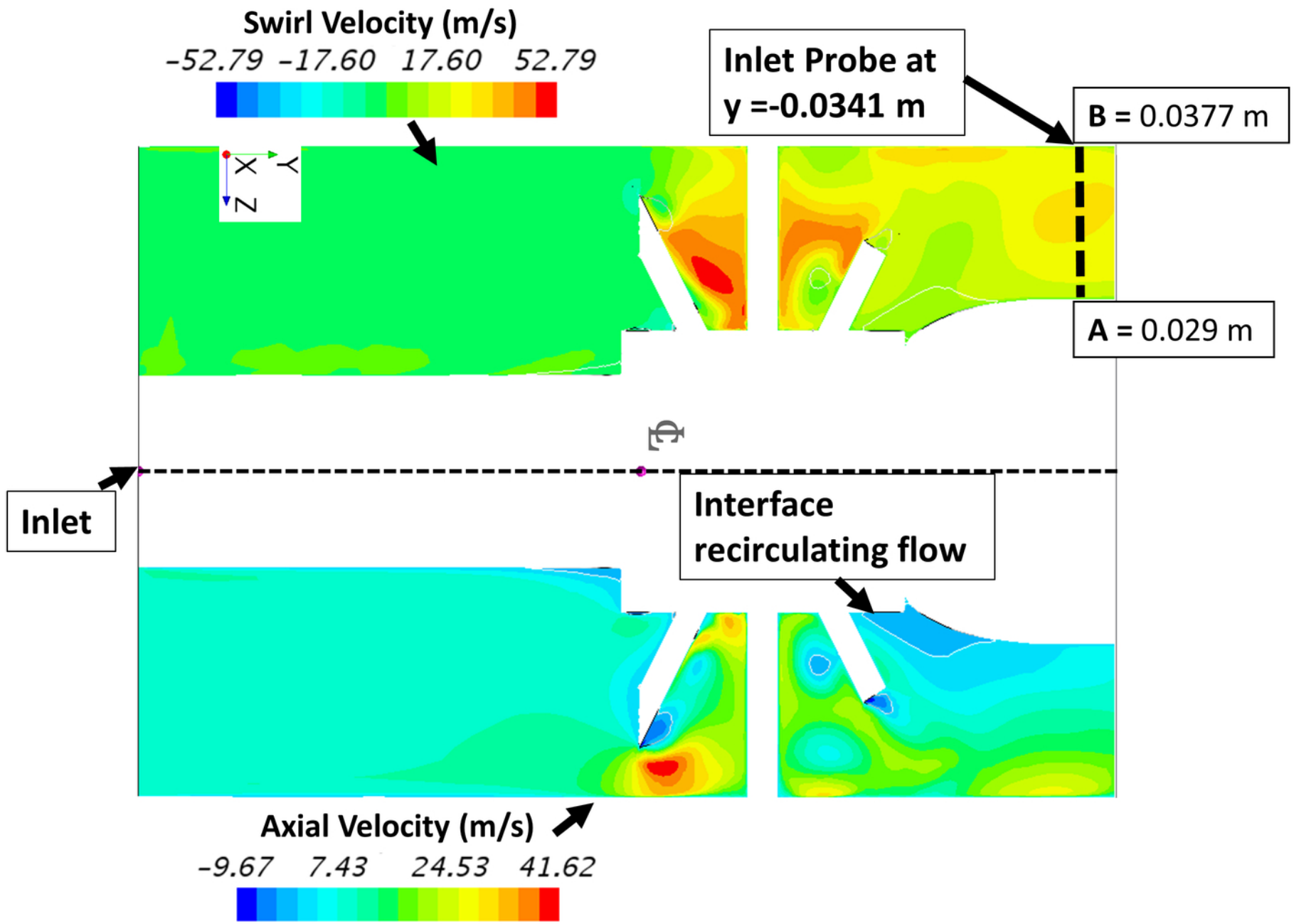
Swirl Velocity (m/s)
-52.79 -17.60 17.60 52.79
Inlet Probe at
y =-0.0341 m
B = 0.0377 m
A = 0.029 m
Inlet
Interface
recirculating flow
Axial Velocity (m/s)
-9.67 7.43 24.53 41.62

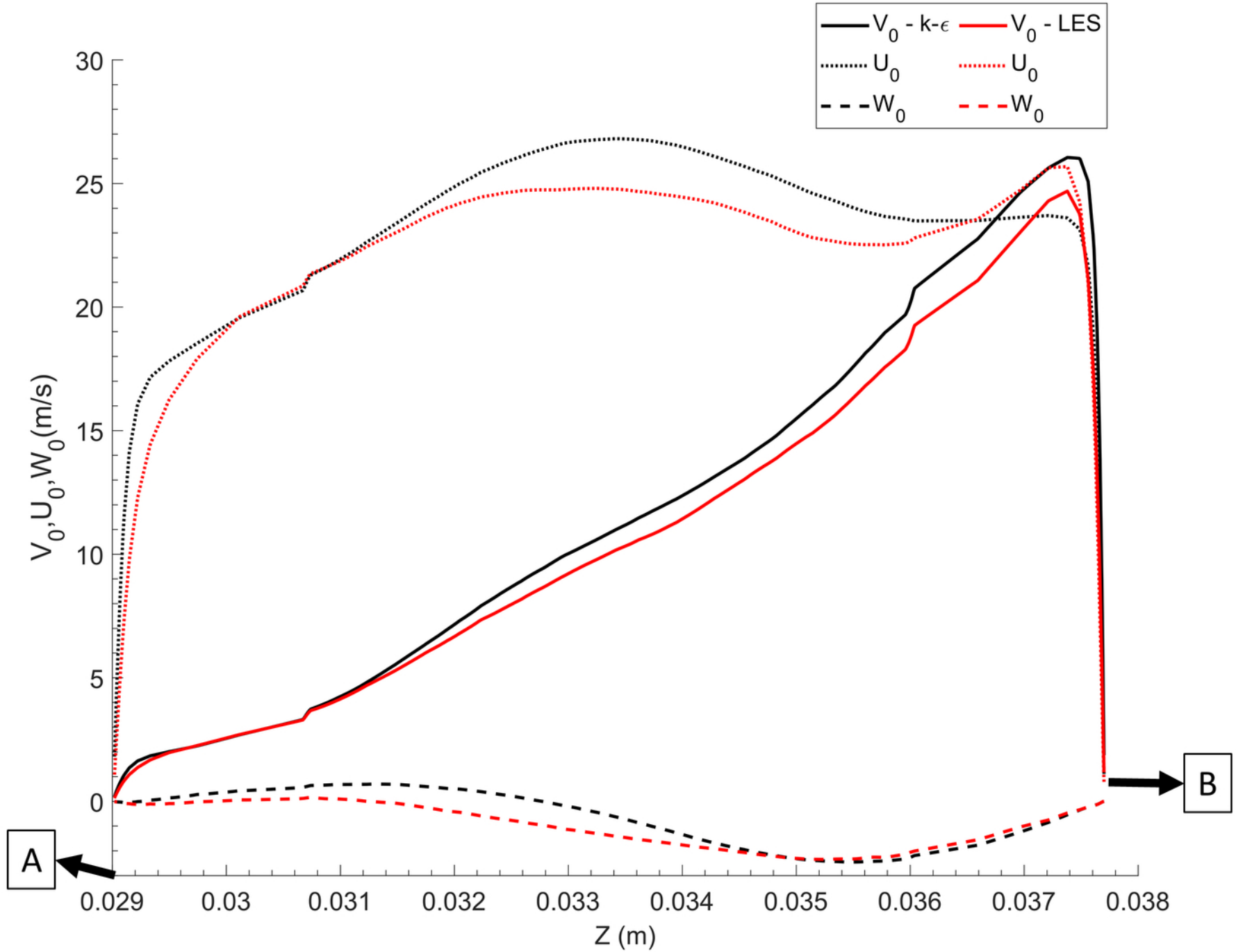
V0 - k-ϵ
V0 - LES
U0
U0
W0
W0
30
25
20
15
10
5
0
V0,U0,W0(m/s)
A
B
0.029
0.03
0.031
0.032
0.033
0.034
0.035
0.036
0.037
0.038
Z (m)

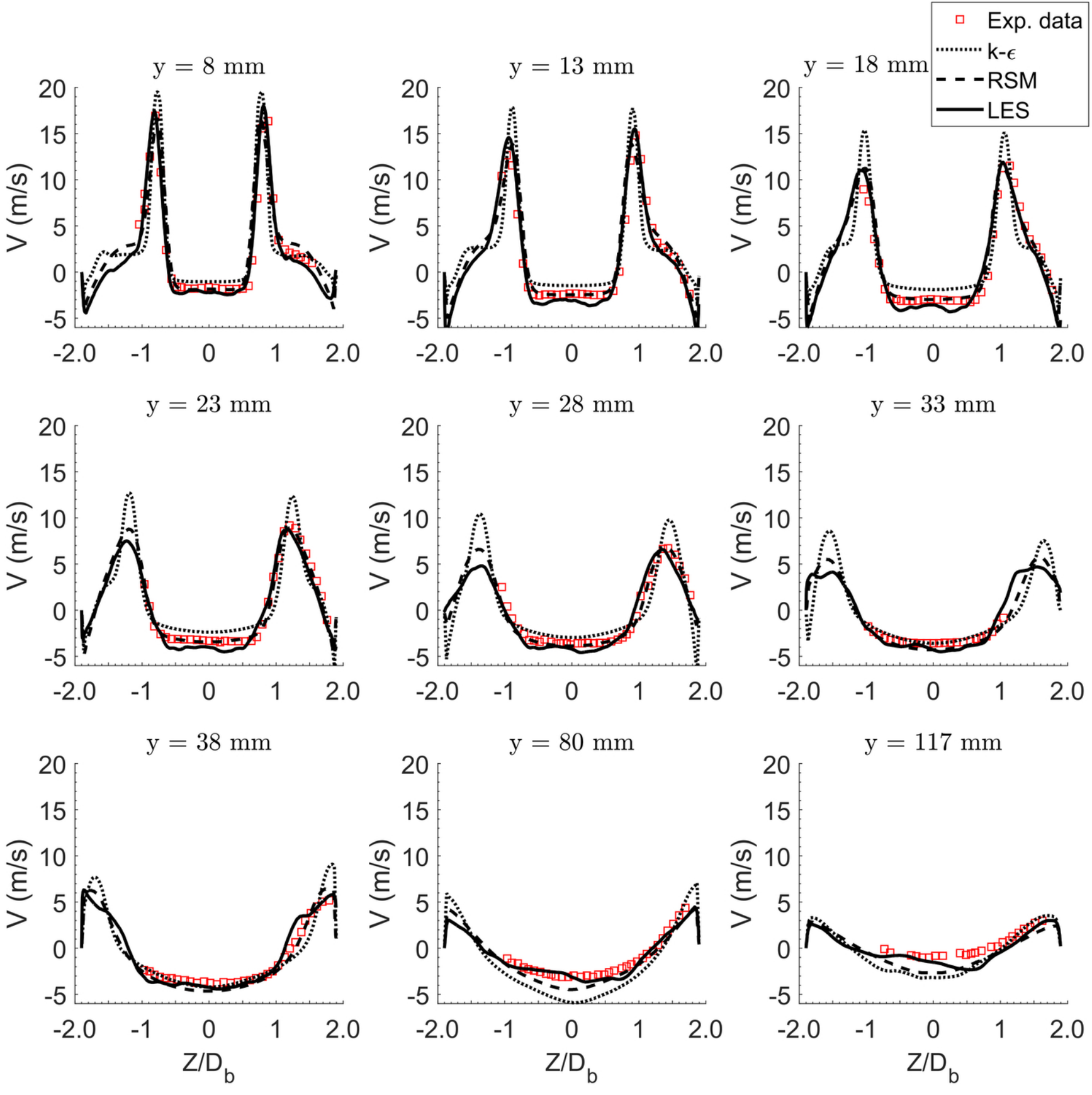
Exp. data
k-ϵ
RSM
LES
y = 8 mm
y = 13 mm
y = 18 mm
y = 23 mm
y = 28 mm
y = 33 mm
y = 38 mm
y = 80 mm
y = 117 mm
V (m/s)
Z/D_b
20
15
10
5
0
-5
-2.0
-1
0
1
2.0

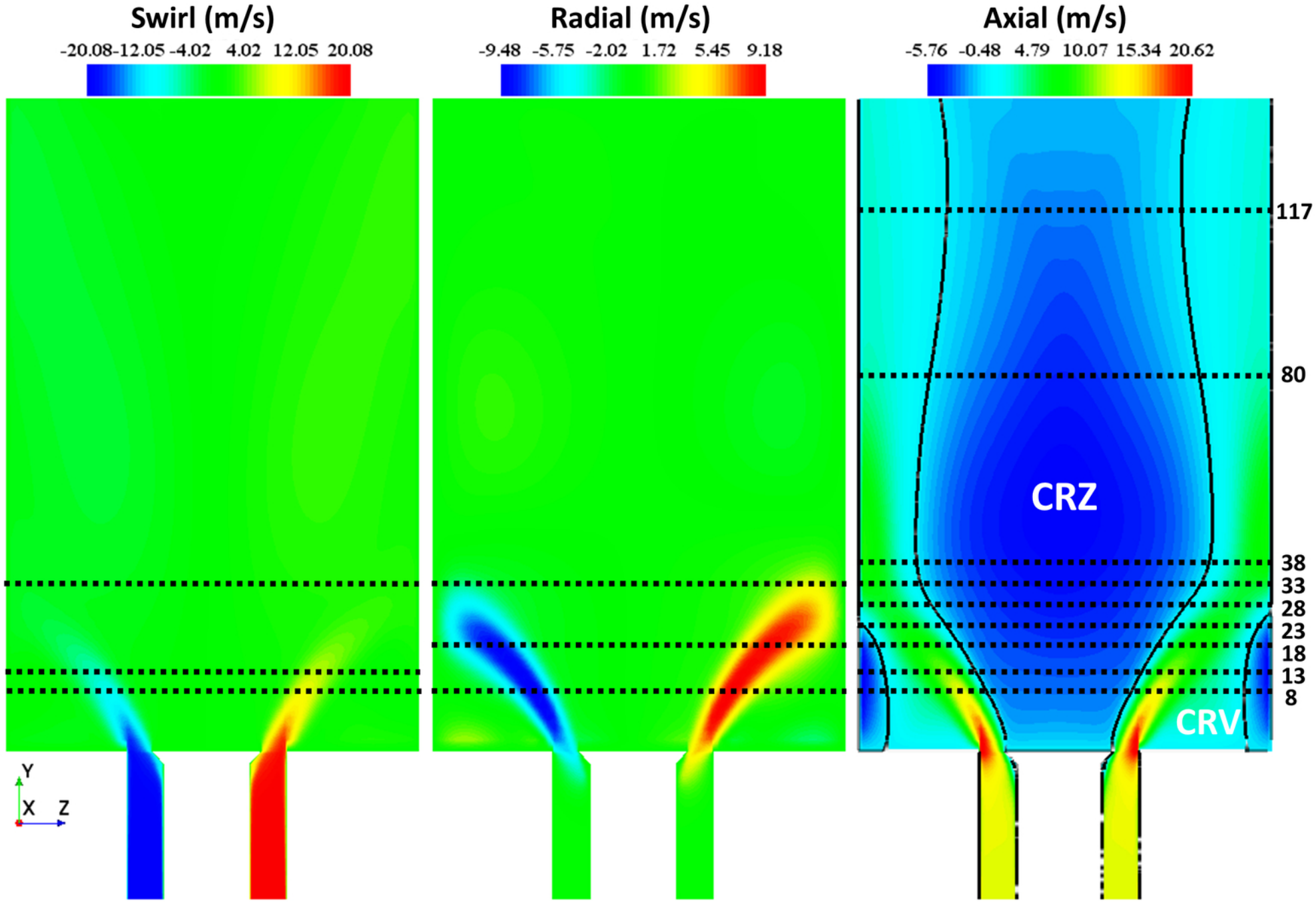
Swirl (m/s)
-20.08 -12.05 -4.02 4.02 12.05 20.08
Radial (m/s)
-9.48 -5.75 -2.02 1.72 5.45 9.18
Axial (m/s)
-5.76 -0.48 4.79 10.07 15.34 20.62
117
80
CRZ
38
33
28
23
18
13
8
CRV
Y
X Z

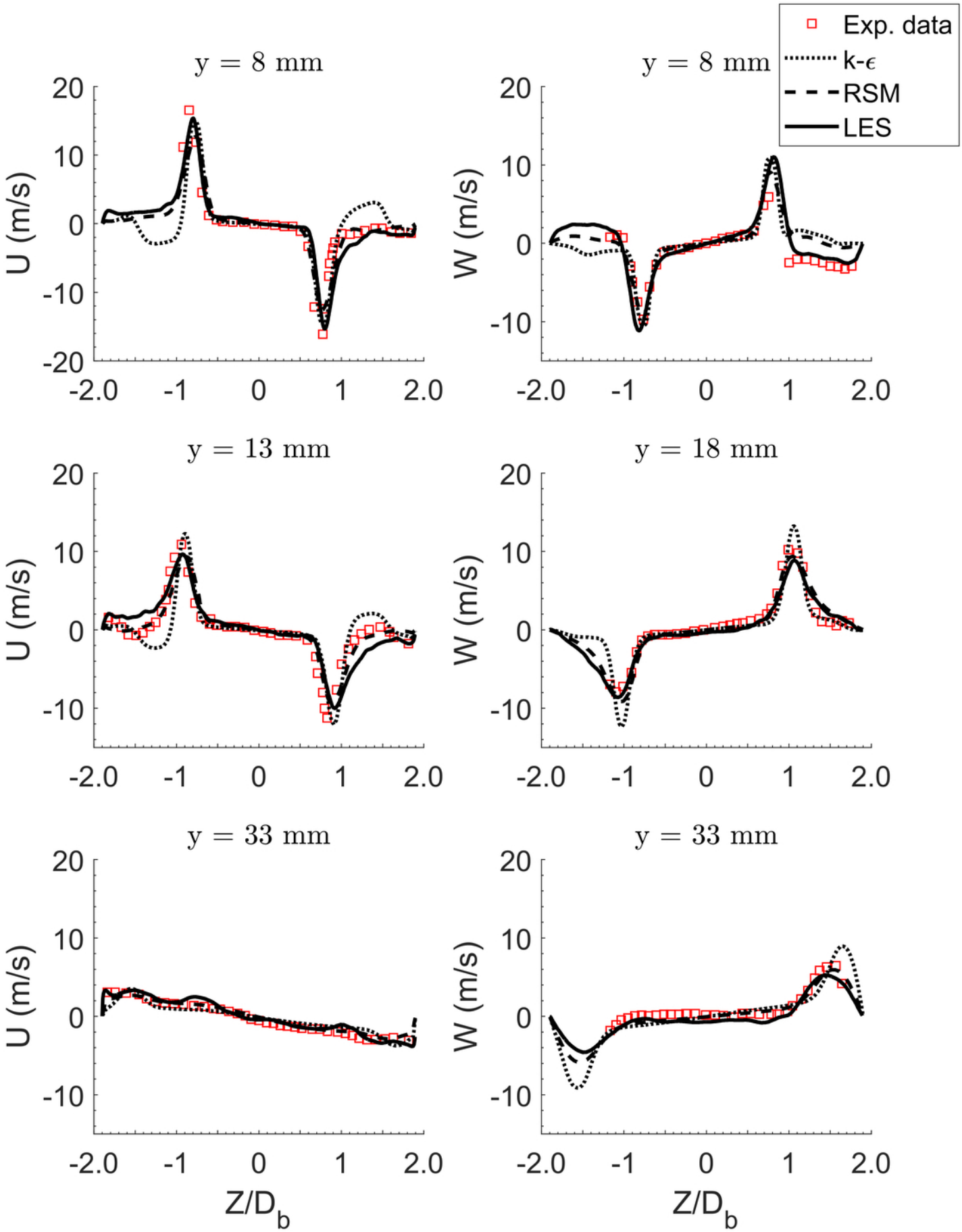
Exp. data
k-ϵ
RSM
LES
y = 8 mm
y = 8 mm
y = 13 mm
y = 18 mm
y = 33 mm
y = 33 mm
U (m/s)
W (m/s)
Z/D_b
20
10
0
-10
-20
-2.0
-1
0
1
2.0

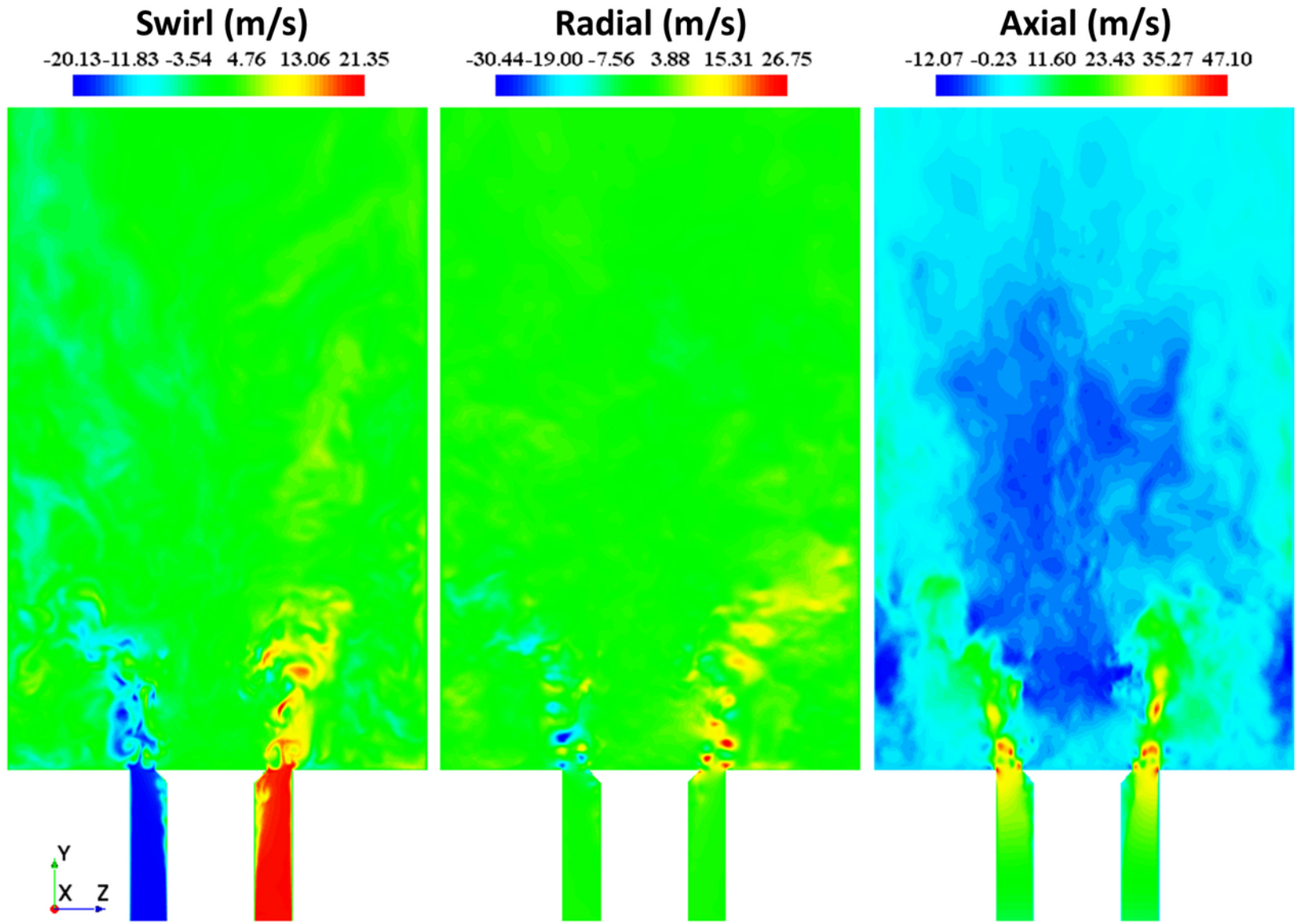
Swirl (m/s)
-20.13 -11.83 -3.54 4.76 13.06 21.35
Radial (m/s)
-30.44 -19.00 -7.56 3.88 15.31 26.75
Axial (m/s)
-12.07 -0.23 11.60 23.43 35.27 47.10
Y
X Z

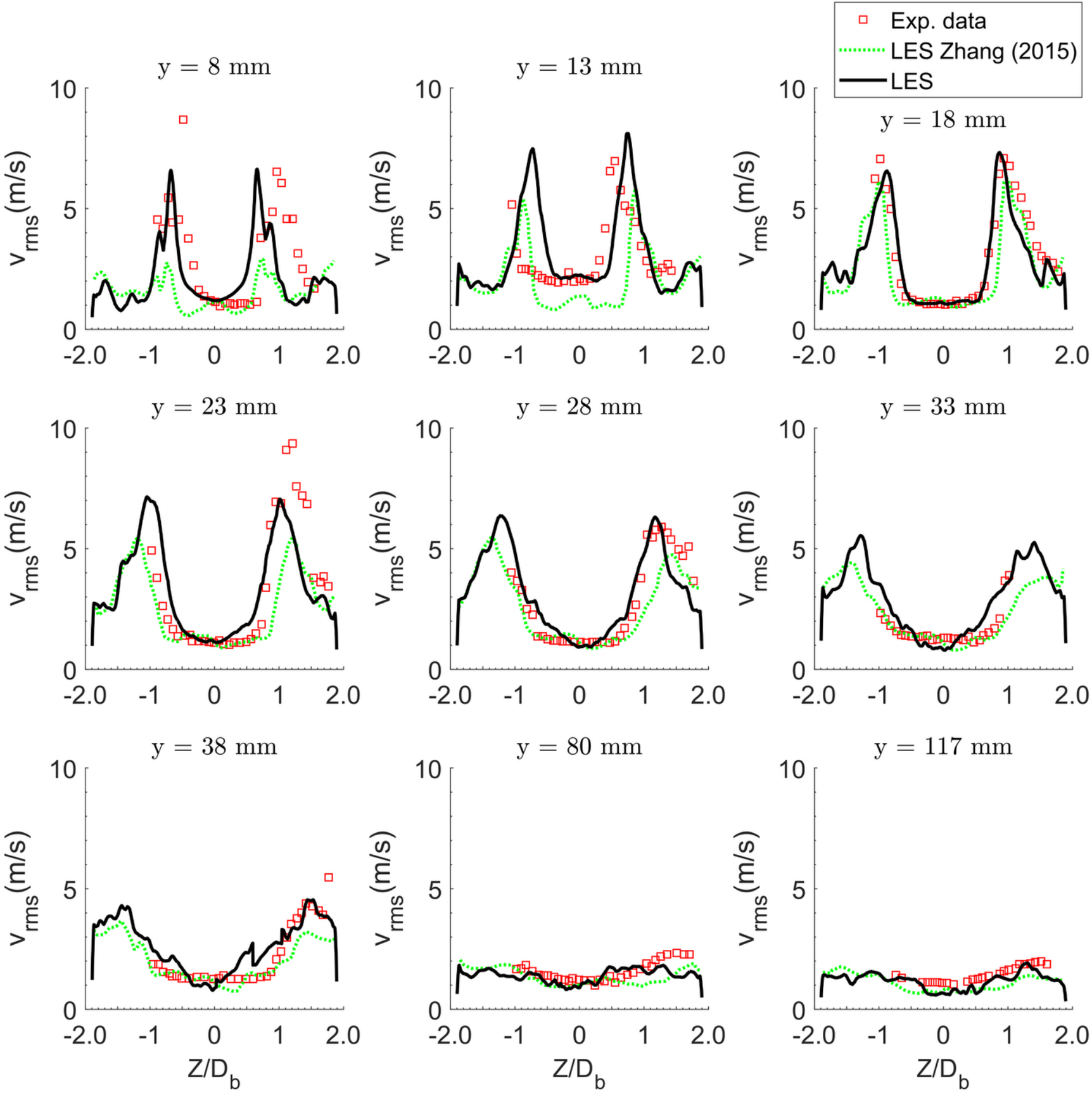
Exp. data
LES Zhang (2015)
LES
y = 8 mm
y = 13 mm
y = 18 mm
y = 23 mm
y = 28 mm
y = 33 mm
y = 38 mm
y = 80 mm
y = 117 mm
v_rms(m/s)
Z/D_b
0
5
10
-2.0
-1
0
1
2.0

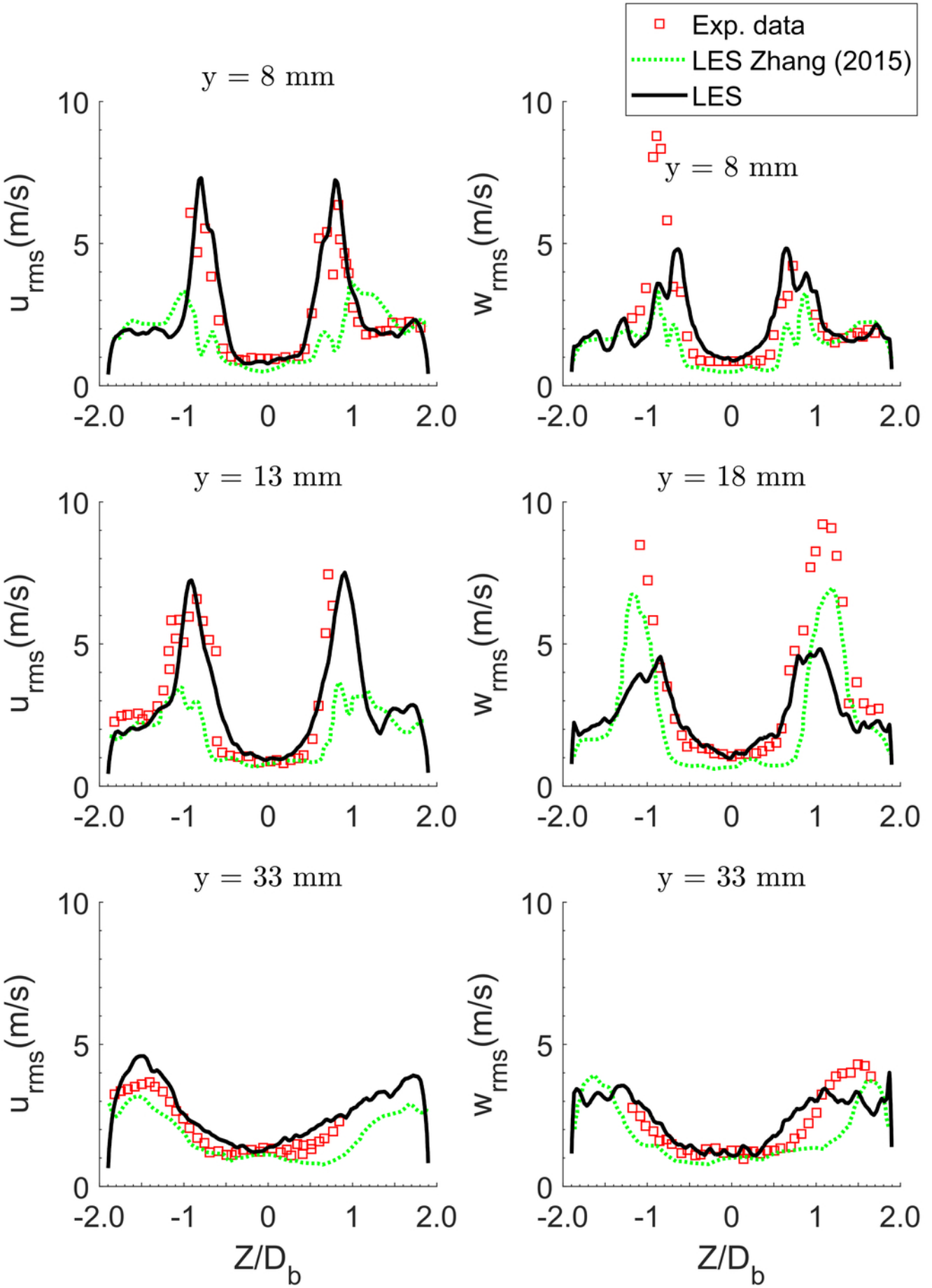
Exp. data
LES Zhang (2015)
LES
y = 8 mm
y = 8 mm
y = 13 mm
y = 18 mm
y = 33 mm
y = 33 mm
u_rms(m/s)
w_rms(m/s)
Z/D_b
Z/D_b
0
5
10
-2.0
-1
0
1
2.0

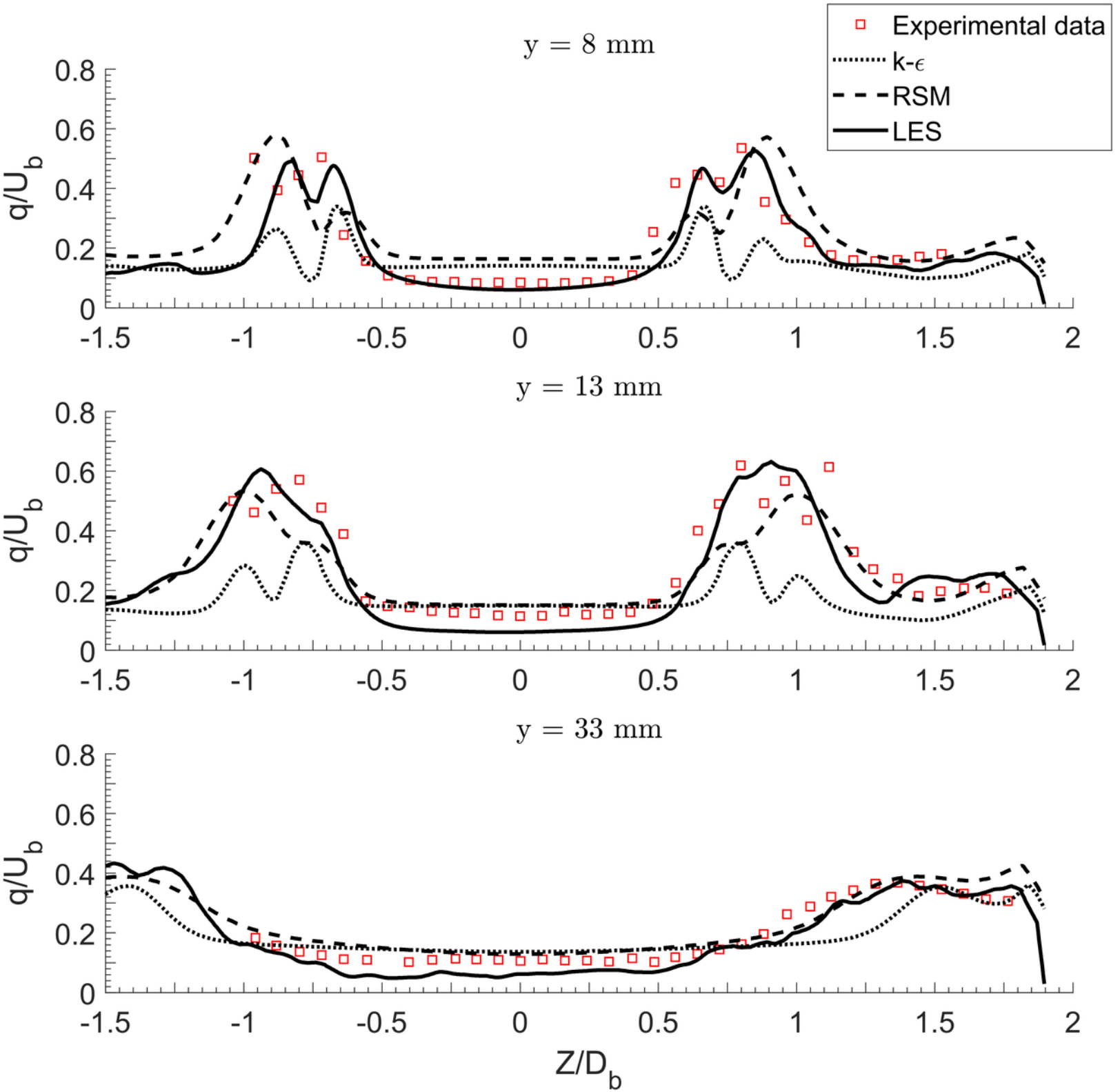
Experimental data
k-ϵ
RSM
LES
y = 8 mm
y = 13 mm
y = 33 mm
q/U_b
Z/D_b
0
0.2
0.4
0.6
0.8
-1.5
-1
-0.5
0
0.5
1
1.5
2

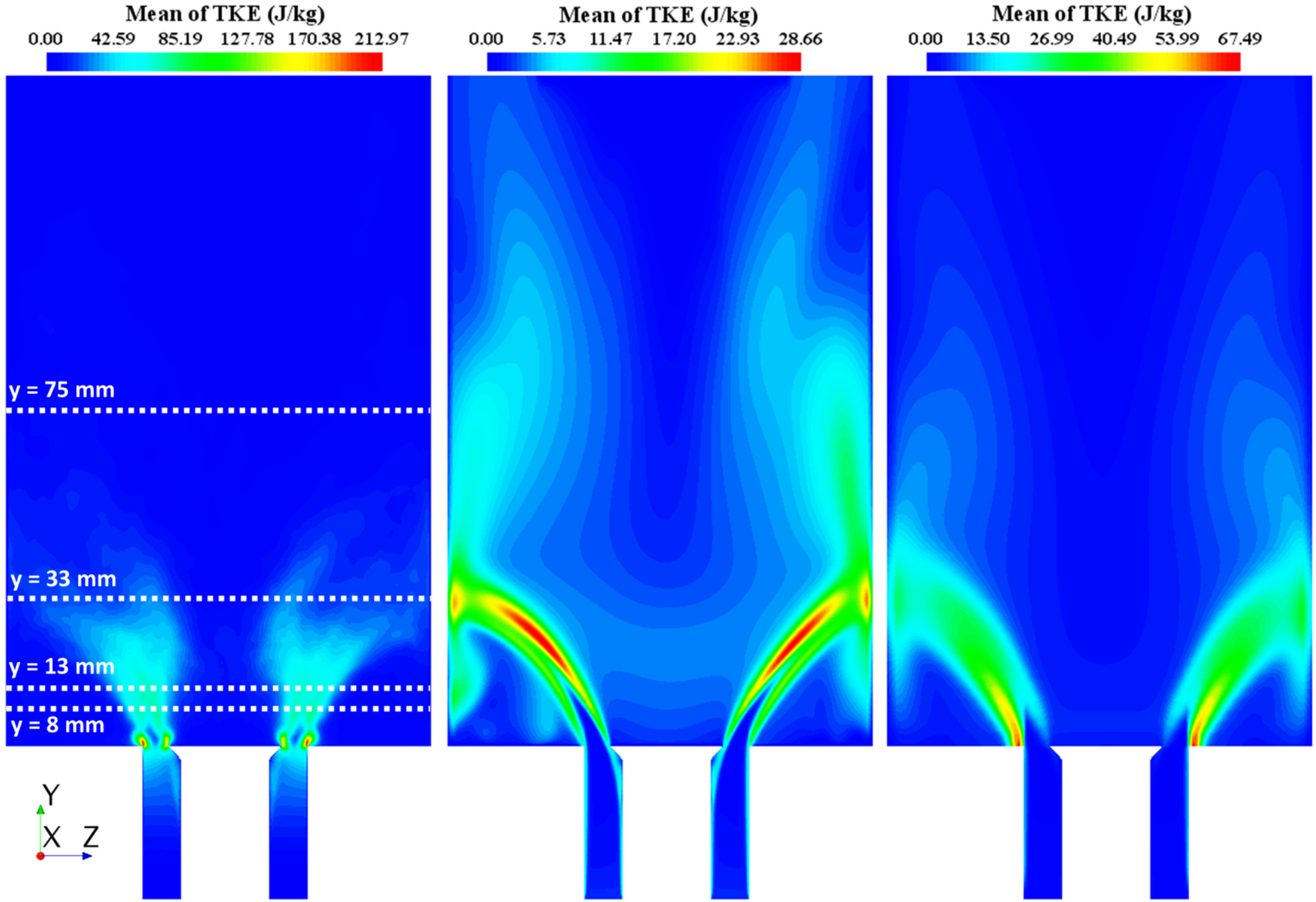
Mean of TKE (J/kg)
0.00 42.59 85.19 127.78 170.38 212.97
Mean of TKE (J/kg)
0.00 5.73 11.47 17.20 22.93 28.66
Mean of TKE (J/kg)
0.00 13.50 26.99 40.49 53.99 67.49
y = 75 mm
y = 33 mm
y = 13 mm
y = 8 mm
Y
X Z

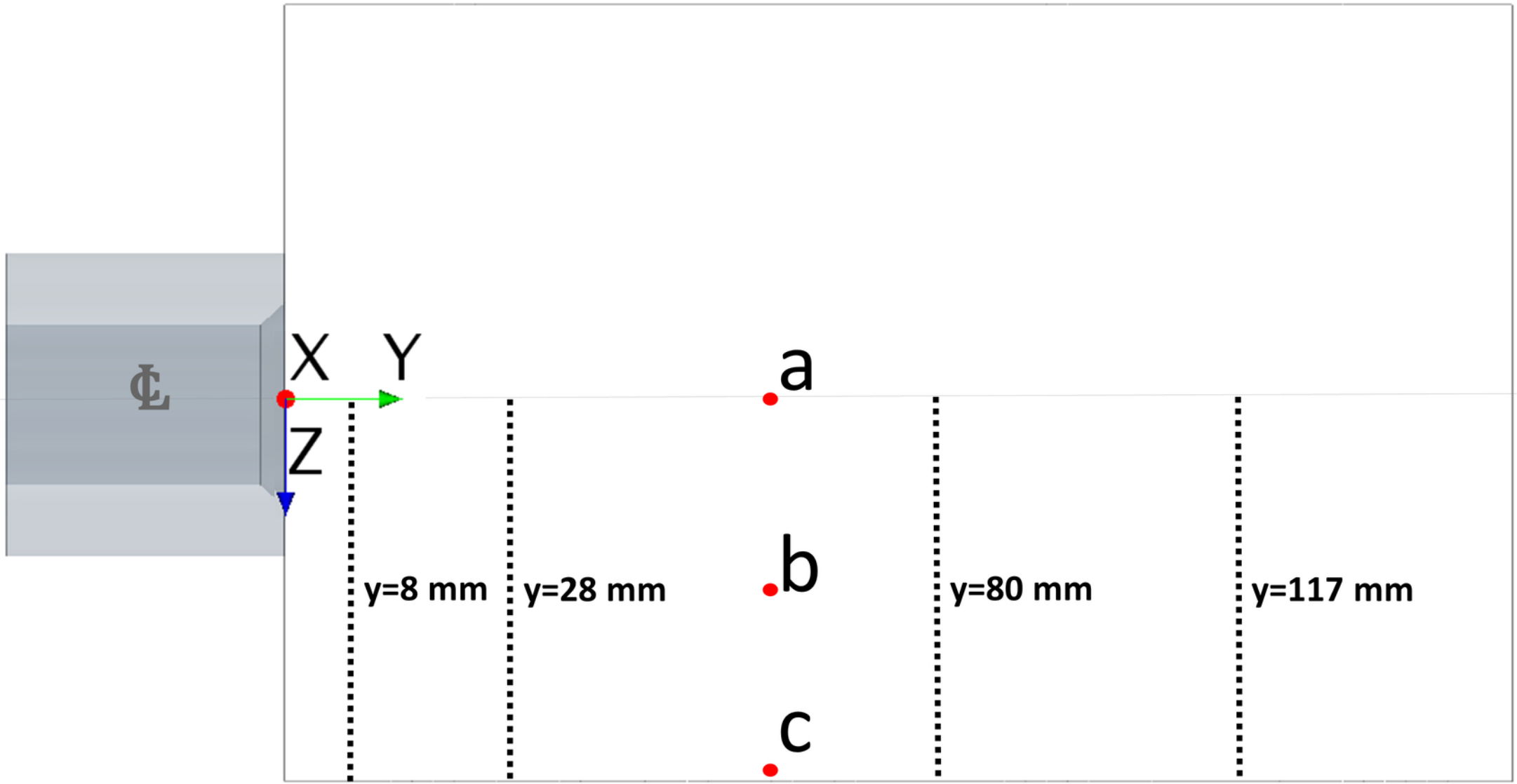
X
Y
Z
a
b
c
y=8 mm
y=28 mm
y=80 mm
y=117 mm

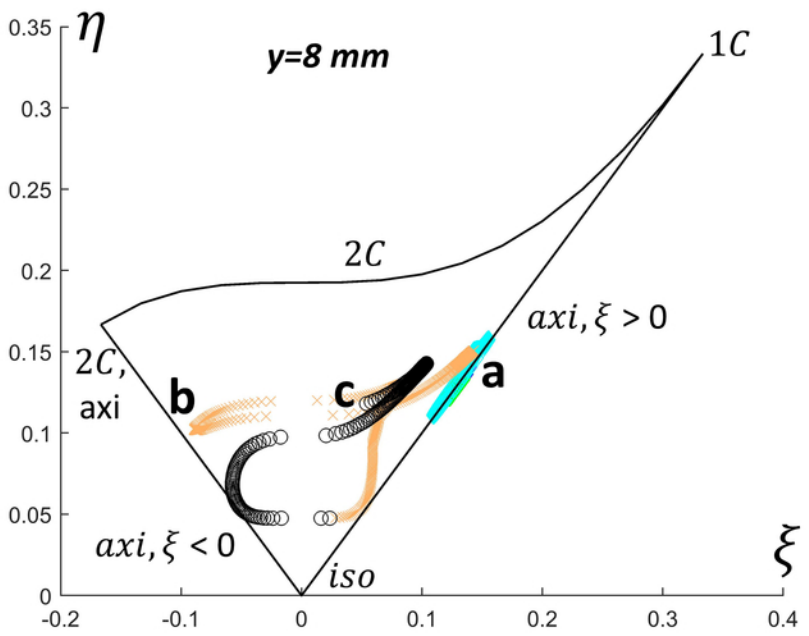
η
y=8 mm
1C
2C
2C, axi
axi, ξ > 0
axi, ξ < 0
iso
a
b
c
ξ

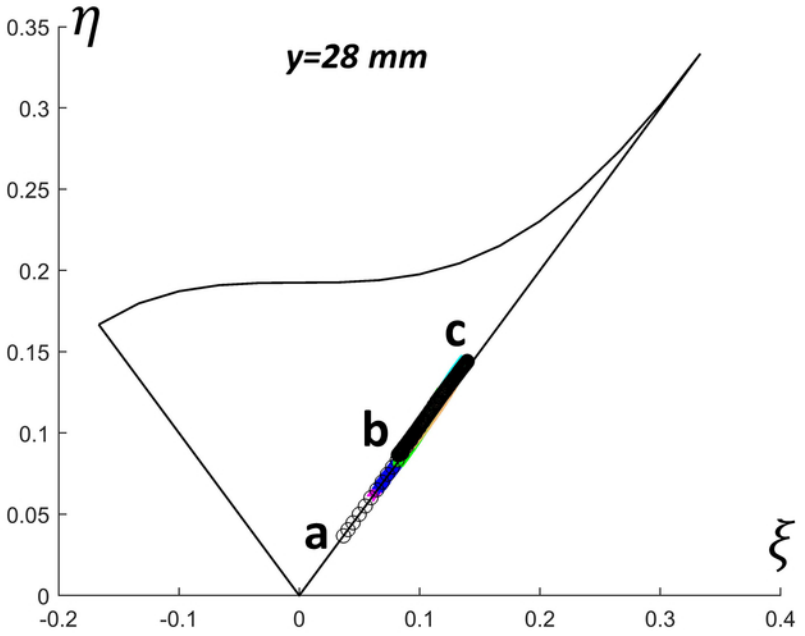
η
y=28 mm
a
b
c
ξ

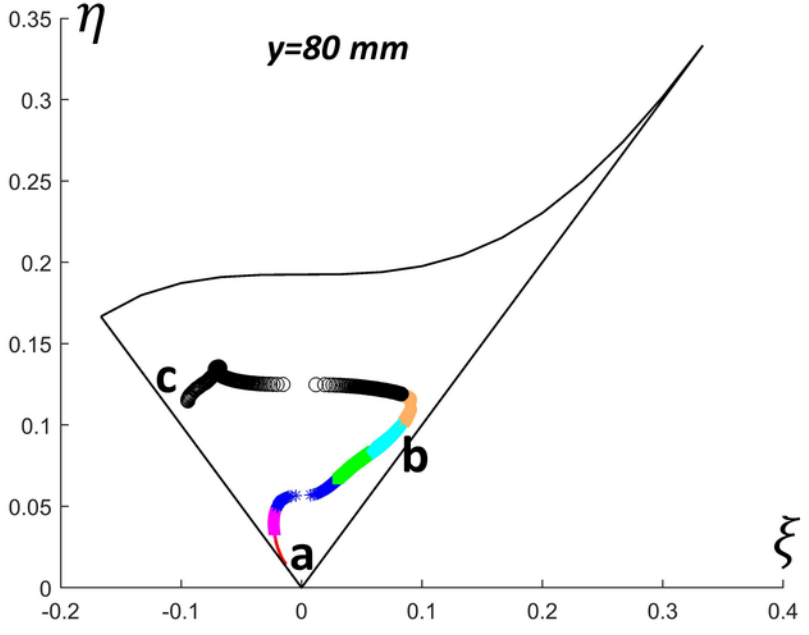
η
y=80 mm
a
b
c
ξ

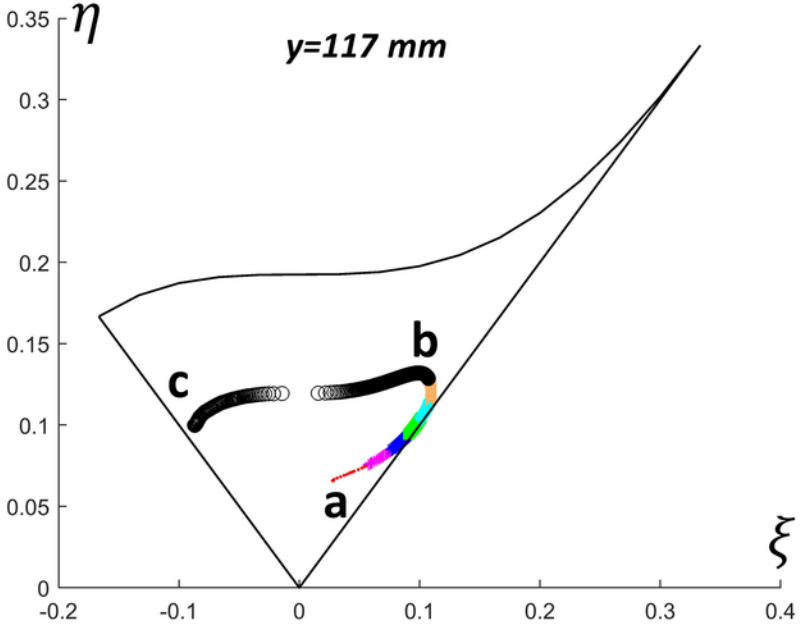
η
y=117 mm
a
b
c
ξ

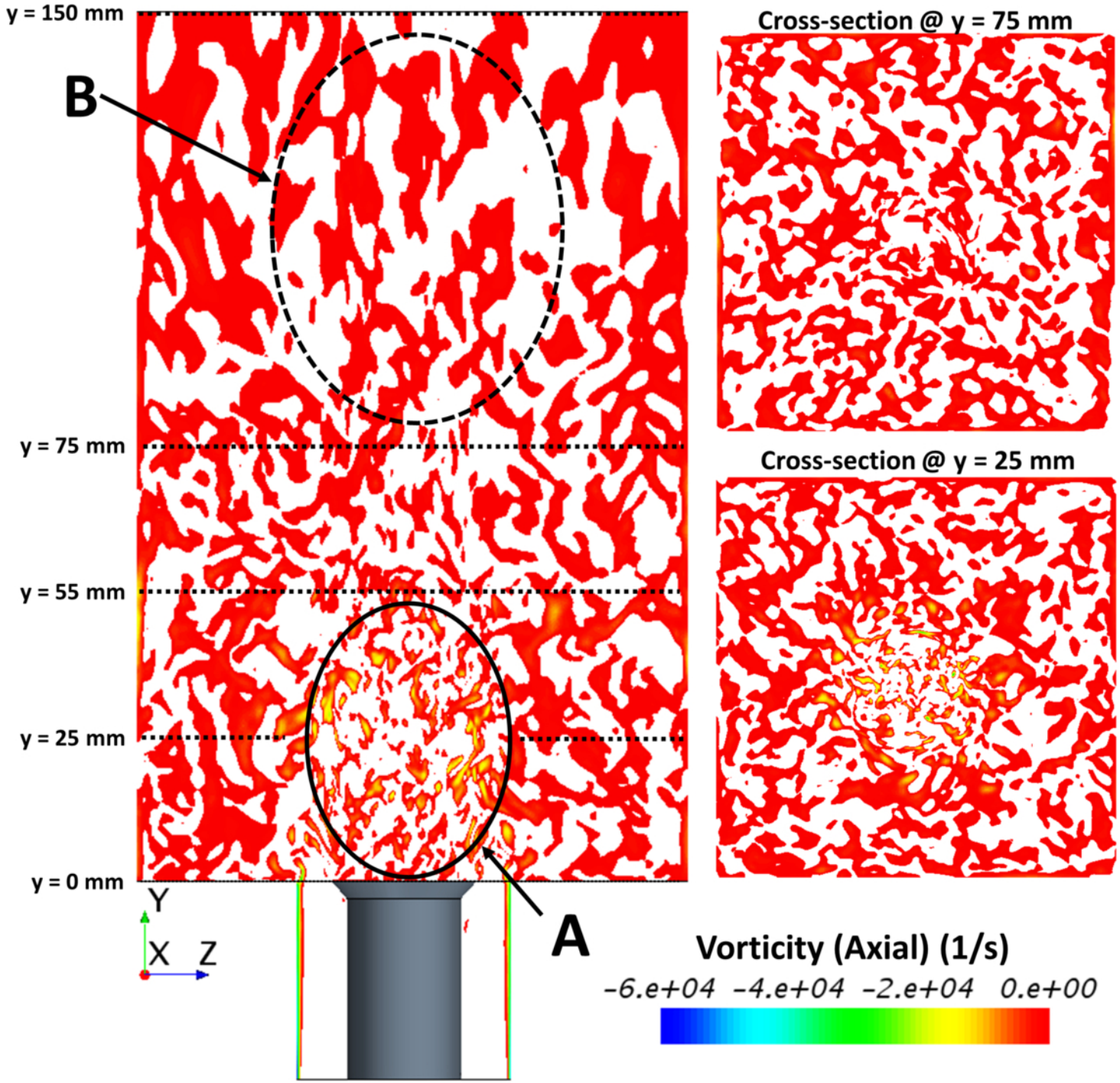
y = 150 mm
B
y = 75 mm
y = 55 mm
y = 25 mm
y = 0 mm
Y
X Z
A
Cross-section @ y = 75 mm
Cross-section @ y = 25 mm
Vorticity (Axial) (1/s)
-6.e+04 -4.e+04 -2.e+04 0.e+00

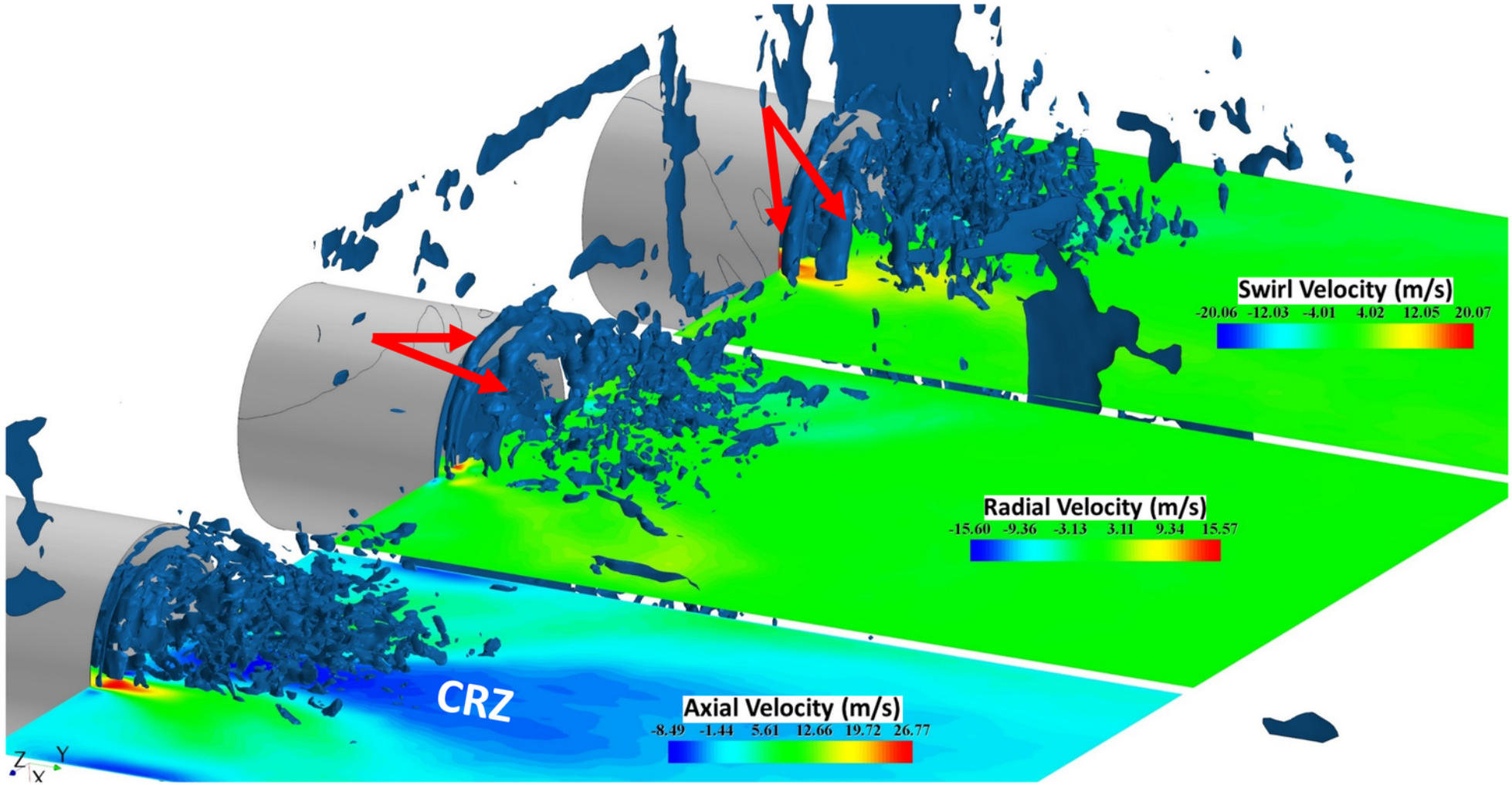
Swirl Velocity (m/s)
-20.06 -12.03 -4.01 4.02 12.05 20.07
Radial Velocity (m/s)
-15.60 -9.36 -3.13 3.11 9.34 15.57
Axial Velocity (m/s)
-8.49 -1.44 5.61 12.66 19.72 26.77
CRZ
Z
Y
X

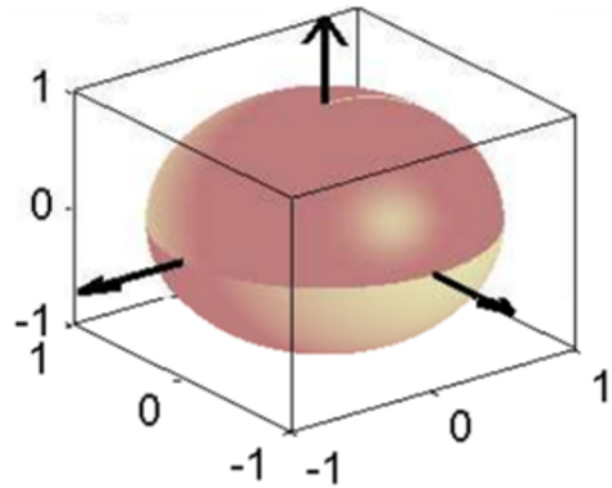
1
0
-1
1
0
-1
-1
0
1

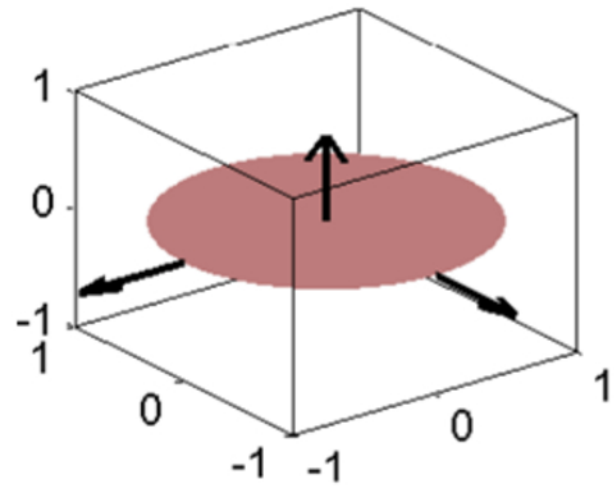
1
0
-1
1
0
-1
-1
0
1

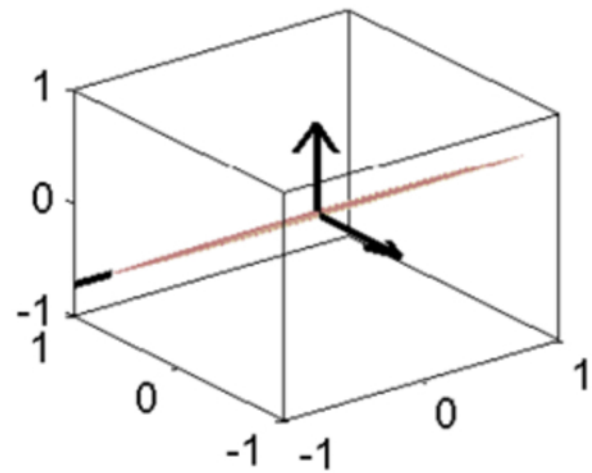
1
0
-1
1
0
-1
-1
0
1

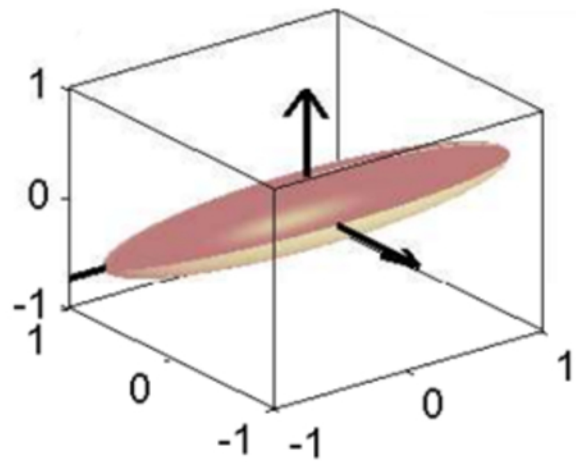
1
0
-1
1
0
-1
-1
0
1

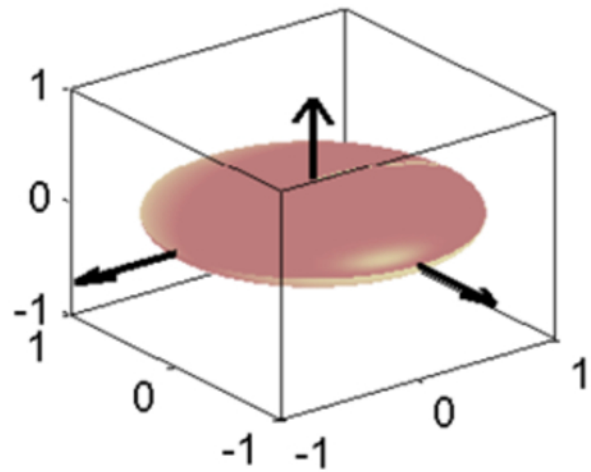
1
0
-1
1
0
-1
-1
0
1

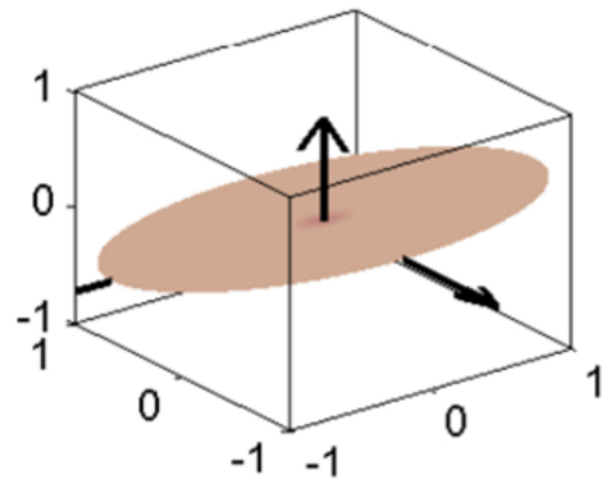
1
0
-1
1
0
-1
-1
0
1